Boundary-Layer Meteorology (2026) 192:29
https://doi.org/10.1007/s10546-026-00969-6

RESEARCH ARTICLE

Structure–Function Parameters Over Different Surface Footprints in Coastal Zones

Andrey A. Grachev[1] · Harindra J. S. Fernando[2] · Stef L. Bardoel[2,3] · Robb M. Randall[1] · Christopher M. Hocut[1] · Edward D. Creegan[1] · Laura S. Leo[2,4]

Received: 14 August 2025 / Accepted: 3 March 2026 / Published online: 29 April 2026

Abstract
High frequency turbulent data from sonic anemometers and other ancillary information collected at multiple levels on several meteorological flux towers located at two coastal sites are used to study velocity and scalar (temperature and humidity) structure–function parameters over heterogeneous surfaces in an area of complex coastal terrains. Understanding of such parameters has important applications for studies on wave propagation in a turbulent atmosphere. One observational site was located on the Outer Banks near the town of Duck, North Carolina, with data from the CASPER-East Program (October–November 2015). The second site was located near the town of Ferryland, Newfoundland, Canada, with data from the C-FOG (Coastal-Fog) field campaign (September–October 2018). These measurements allowed studies of structure parameters and other statistics for different footprints, including relatively smooth sea surface conditions and aerodynamically rough dry inland areas for both stable and unstable stratifications. The coastal land cover discontinuity for onshore and offshore winds leads to a thin internal boundary layer (IBL) that could often be resolved by the instrumented towers. The drag coefficient, Bowen ratio, and diurnal variation of sensible heat flux were found to be coastal IBL markers. Our study shows that lower values of the dimensional structure parameters are associated with higher altitudes, smooth surfaces (i.e., over water, outside onshore IBL) and stable stratification (e.g., nocturnal boundary layer), ceteris paribus. In particular, observations showed that the structure parameters over land footprint areas (inside the onshore IBL) can be an order of magnitude larger than over the sea surface due to the change of aerodynamic and thermal properties of the surface. This study also discusses the applicability of Monin–Obukhov similarity theory (MOST) for the velocity and scalar structure parameters in the coastal environment for both stable and unstable conditions. While surface inhomogeneities and the complexity of the coastal landforms nominally violate assumptions underlying MOST, our observations show that the nondimensional structure parameters obey MOST reasonably well for all measurement levels, stability condition, and wind direction. In addition, we suggest a new variance-based hybrid scaling for the structure parameters that overcomes some of the shortcomings of the traditional approach (e.g., self-correlation and ambiguity of the dimensionless temperature structure parameter for near-neutral conditions).

Extended author information available on the last page of the article

Keywords Coastal zone · Flux footprints · Internal boundary layer · Monin–Obukhov similarity theory · Structure parameters

1 Introduction

The primary effects of atmospheric turbulence on wave propagation arise from the spatial and temporal fluctuations of the refractive index of air, n, which is a function of temperature, humidity, pressure and is explicitly dependent on wavelength of a propagating wave, λ, a phenomenon known as dispersion. Changes of the refractive index by atmospheric turbulence is quantified by the structure–function parameter (or just structure parameter) of the refractive index, C_n^2, (defined shortly). Assuming that air pressure fluctuations make a negligible contribution, C_n^2 is directly linked to structure parameters of conserved scalars (temperature, C_T^2, and specific humidity, C_q^2) and velocity because they dictate the fluctuations in the refractive indices of various types of waves propagating in the turbulent atmosphere (Tatarski 1961; Wesely 1976; Kohsiek 1982; Gur'yanov et al. 1987; Andreas 1988, 1989; Fairall 1991; Kaimal and Finnigan 1994; Peltier and Wyngaard 1995; Petenko and Shurygin 1999; Moene 2003; Moene et al. 2004; Beyrich et al. 2005; Meijninger et al. 2006; Hoedjes et al. 2007; Wyngaard 2010; Li et al. 2012; Wood et al. 2013; Petenko et al. 2014; Ostashev and Wilson 2015; Wainwright et al. 2015; Gibbs and Fedorovich 2020a, b; Fiorino et al. 2021; Wang et al. 2020, 2021; Basu and Holtslag 2022 among others).

The refractive index structure parameter is a key parameter for understanding and accurately modelling and predicting the effects of turbulence on the propagation of waves, such as electromagnetic (optical, infrared, radio) and acoustic waves. In particular, C_n^2 is of obvious relevance for telecommunications (including laser communication), imaging systems, adaptive optics, ground-based astronomy, micrometeorology (e.g., scintillometry, remote sensing by Doppler LiDAR), and many other important applications. With knowledge on the structure parameters and other atmospheric turbulence characteristics, it is possible to assess the wave propagation performance. Atmospheric turbulence significantly impacts wave propagation (e.g., laser beams) leading to phenomena like beam broadening and spreading, beam distortion and degradation (e.g., signal loss), scintillation (twinkling), beam wander, and image blur, among other effects (e.g., Fussman 2014; Fahey et al. 2021). Note that the refractive index structure parameter is frequently referred to as the "optical turbulence strength".

Along with C_n^2, the structure parameters of a velocity component and a conserved scalar are widely used in wave-propagation studies but their specific combination that affects a wave depends on the wave's nature. Optical and infrared waves propagating over land are primarily affected by temperature and, to a lesser extent, humidity fluctuations, although over oceans or water-saturated soils, C_n^2 is dominated by C_q^2 or at least the effects of humidity cannot be neglected (Kaimal 1973; Wesely 1976; Kohsiek 1982; Andreas 1988; Fairall 1991; Moene 2003). For radio wavelengths, the humidity field is also required to produce an estimate of the refractive index structure parameter (e.g., Frehlich et al. 2010). Sound (acoustic) waves are mechanical waves and the index of refraction of sound waves is affected by both velocity and scalar structure parameters (Kaimal 1973; Ostashev and Wilson 2015).

There are various methods for estimating C_n^2 in turbulent atmosphere, including direct measurements between two points (e.g., Gur'yanov et al. 1987) and estimates by scintillometers and sonic anemometer/thermometer plus fast-response gas analyser. Scintillometry is a common method for measuring C_n^2 by detecting the intensity fluctuations of a light beam transmitted across a path (e.g., Moene et al. 2004 and references therein). Scintillometers measure a path-averaged value of the refractive index structure parameter, C_n^2. Sonic anemometers provide point measurements of the structure parameters of a velocity component and sonic-temperature structure parameter, C_T^2. To evaluate the moisture structure parameter, C_q^2, high-speed open-type gas analysers are required. Because C_n^2 is generally a function of C_T^2, C_q^2, their cross-structure parameter, and λ, it is possible to estimate C_n^2 from measurements of the scalar structure parameters and vice versa (see Sect. 2.3 below). Methods for estimating the structure parameters from sonic anemometer data include, among others, the two-point structure function method based on the definition of C_n^2 and spectral analysis assuming a –5/3 Kolmogorov power law in the inertial subrange. A comparison of C_T^2 estimated by sonic anemometer and scintillometer shows generally good agreement (e.g., Beyrich et al. 2005; Meijninger et al. 2006; Hoedjes et al. 2007; Wood et al. 2013; Perelet et al. 2022).

Turbulence measurements in a coastal zone considered in this study may provide valuable information on wave propagation near the surface over different footprints for both stable and unstable stratifications. There is a long history of studying coastal zones with a focus on small-scale turbulence, and the literature on the subject is voluminous with numerous global coastal zone classifications (e.g., Garratt 1987, 1990; Garratt and Ryan 1989; Mahrt et al. 1998a, 2016, 2021; Vickers and Mahrt 1997, 2010; Sun et al. 2001; Vickers et al. 2001; Geernaert 2002; Fairall et al. 2006; Grachev et al. 2011, 2018a, 2021; Ortiz-Suslow et al. 2018, 2021; Ortiz-Suslow and Wang 2019; Petenko et al. 2020; Alappattu et al. 2022; Krishnamurthy et al. 2023; Bardoel et al. 2025; Potter et al. 2025, and references therein). Turbulent measurements in a coastal zone can provide valuable information on statistics needed for many applications as stated above, but the measurements are onerous due to the complexity of coastal environments. Limited available small-scale turbulence observations in coastal zones have been a bane for validation and calibration of models for structure parameters.

This study seeks to advance our understanding of the structure parameters under conditions that strongly violate the fundamental assumptions underlying the MOST (over heterogeneous surfaces in an area of complex coastal landforms), and when the non-dimensional profiles of wind speed and temperature fail to predict fluxes correctly, e.g., vertical turbulent fluxes may contradict local gradients (Grachev et al. 2018a, Figs. 14 and 15). The structure parameters are derived here from sonic anemometer/thermometer and fast-response open path infrared gas analyser based on the spectral approach. The data were collected (i) at the North Carolina's Outer Banks coastal zone near the town of Duck during the Coupled Air-Sea Processes and EM Ducting Research (CASPER) program in October–November 2015 (e.g., Grachev et al. 2018a; Wang et al. 2018) and (ii) near the town of Ferryland on the Avalon Peninsula, Newfoundland, Canada during the C-FOG (Coastal Fog) field program in September–October 2018 (e.g., Bardoel et al. 2021; Dorman et al. 2021; Fernando et al. 2021; Grachev et al. 2021; Perelet et al. 2021).

The paper is organized as follows. Section 2 provides a formal background of the structure parameter and coastal IBLs. Section 3 introduces CASPER-East and C-FOG observation sites, instrumentation and the datasets. The main findings based on experimental data collected at these two coastal sites are described in Sect. 4 (coastal IBL markers, time series, and similarity functions of the structure parameters). Concluding remarks are given in Sect. 5. Some material presented in the current study, e.g., description of the observation sites, instrumentation, and data sets (Sect. 3), is partially repeated here from Grachev et al. (2018a) and

Grachev et al. (2021). These studies used the same CASPER-East and C-FOG datasets but to address different problems.

2 Background Information

In this section, we define the structure parameter of a velocity component and a conserved scalar and describe Monin–Obukhov's framework for structure parameters.

2.1 Structure Parameter Formulation

Historically the structure parameter of some fluctuating atmospheric variable α was defined in terms of the second-order structure function $D_\alpha(r)$ (Tatarski 1961; Kaimal and Finnigan 1994; Wyngaard 2010):

$$D_\alpha(r) = \overline{[\alpha'(x) - \alpha'(x+r)]^2}, \tag{1}$$

where α ($= u, v, w, T, q$, and n) denotes the longitudinal, lateral, vertical velocity components, temperature, specific humidity, and refractive index of air, respectively, and r is the distance separating two measurement points of α along the x axis. Here the prime [′] denotes fluctuations about the mean value, and an overbar is an averaging operator. In the atmospheric boundary layer, the relationship for $D_\alpha(r)$ at small size scales is based on Kolmogorov's (1941) fundamental theory of locally isotropic turbulence. Assuming turbulence is locally isotropic and that r lies within the inertial subrange of spatial scales of turbulent fluctuations, (1) based on Kolmogorov's (1941) similarity hypotheses may be expressed as:

$$D_\alpha(r) = C_\alpha^2 r^{2/3} : \tag{2}$$

where C_α^2 is the structure parameter, which is assumed constant within the inertial subrange associated with the Richardson-Kolmogorov cascade.

In turn, C_α^2 may be related to the one-dimensional inertial subrange wavenumber spectrum of the corresponding variable α:

$$F_\alpha(k) = c_0 C_\alpha^2 k^{-5/3}, \tag{3}$$

where k is the wavenumber and c_0 a constant. According to Wyngaard et al. (1971) the proportionality coefficient in (3) $c_0 = 0.25$ (see also Kaimal 1973; Kaimal and Finnigan 1994; Wilson and Fedorovich 2012; Maronga et al. 2013, 2014; Gibbs et al. 2016 among others). However, Gibbs and Fedorovich (2020a, b) recently demonstrated that the coefficient originally presented by Wyngaard et al. (1971) is too large by a factor of two, i.e., this coefficient should be $c_0 = 0.125$ (see Gibbs and Fedorovich 2020a, b and references therein). Gibbs and Fedorovich (2020a, b) remarked that this disparity lies in the fact that different methods (direct and spectral) are used to evaluate structure parameters in observational, modelling and numerical (e.g., LES) studies (Gibbs et al. 2016). Specifically, this depends on the limits of integration (from 0 to $+\infty$ or from $-\infty$ to $+\infty$) used in a particular program for the relationship between the structure function and the one-dimensional spectral density of turbulent fluctuations.

Spatial scales and the wavenumber spectrum $F_\alpha(k)$ in (3) should be converted, respectively, into frequency scales and the frequency spectrum $S_\alpha(f)$ because most measurements including C_α^2 are performed in the frequency space (e.g., by traditional sonic anemometer/thermometer measurements). The frequency $S_\alpha(f)$ and wavenumber $F_\alpha(k)$ spectra are related to each other through $fS_\alpha(f) = kF_\alpha(k)$ (Kaimal and Finnigan 1994). By using Taylor's frozen turbulence hypothesis, $k = 2\pi f/U$ (where f is frequency and U the mean wind speed), the wavenumber spectrum in the inertial subrange (3) can be re-written in terms of frequency as follows:

$$S_\alpha(f) = c_0 C_\alpha^2 (U/2\pi)^{2/3} f^{-5/3}. \tag{4}$$

In the current study, Eq. 4 is used to estimate structure parameters from sonic anemometer data (Sect. 4). Note that the variance σ_α^2 is the integral of the spectrum $S_\alpha(f)$ over the entire frequency range from 0 to ∞ (or the integral of the spectrum $F_\alpha(k)$ over all wavenumbers):

$$\sigma_\alpha^2 = \int_0^\infty S_\alpha(f)df = \int_0^\infty F_\alpha(k)dk. \tag{5}$$

The main contribution to σ_α^2 is associated with the energy-containing range where energy is produced by buoyancy and shear (e.g., Kaimal and Finnigan 1994), whereas the structure parameter C_α^2 is linked to the contribution to σ_α^2 in the inertial subrange (cf. Equation 3–5). However, the magnitude of C_α^2 in the inertial subrange is inextricably linked to the spectral maximum associated with the energy-containing turbulent eddies (i.e., linked to σ_α^2). For example, in Kaimal's (1973) model, this is realized through the frequency scale f_0 (see Fig. 1 and Eq. 3 in Kaimal 1973). In other words, it can be assumed that C_α^2 is strongly correlated with σ_α^2 mainly due to this reason (also see below Sect. 4.4). Recall that according to the Richardson-Kolmogorov's concept, turbulent energy in the inertial subrange cascades down from the energy-containing to smaller scales where it is dissipated and the turbulence production and dissipation terms balance each other under the equilibrium conditions (e.g., Kaimal and Finnigan 1994). For example, higher production rate of the turbulent energy (i.e., higher σ_α^2) is associated with higher dissipation rate and, therefore, this requires the higher energy cascade rate in the inertial subrange (i.e., higher C_α^2). Note that Högström et al. (2002) reported that large-scale detached eddies originating from the upper layers of the atmospheric boundary layer can impact velocity variances (mainly σ_w^2/u_*^2) and the low-frequency parts of the appropriate velocity spectra at high Reynolds number during near-neutral conditions.

According to the similarity hypotheses presented in Kolmogorov (1941), the velocity structure parameters yield $C_{\alpha_V}^2 \propto \varepsilon^{2/3}$, here $\alpha_V = u, v, w$ and ε is the dissipation rate of turbulent kinetic energy (TKE). The frequency energy spectrum of the longitudinal velocity component, $S_u(f)$, in the inertial subrange has the form (cf. Equation 4):

$$S_u(f) = \alpha_K (U/2\pi)^{2/3} \varepsilon^{2/3} f^{-5/3}, \tag{6}$$

where α_K is the Kolmogorov constant with a value estimated $\alpha_K \approx 0.5$–0.6 (e.g., Kaimal and Finnigan 1994); a value $\alpha_K = 0.55$ is adopted in our study. Note that, in contrast to Eq. 4, Eq. 6 does not directly depend on the value of the proportionality coefficient c_0 in Eq. 3 (one can say that this coefficient is included in α_K). If the turbulence is locally isotropic, the longitudinal and transverse (lateral and vertical) velocity structure parameters are related as:

$$C_v^2 = C_w^2 = (4/3)C_u^2. \tag{7}$$

According to the Obukhov-Corrsin law for a passive scalar, the scalar structure parameters yield $C^2_{\alpha_S} \propto N_{\alpha_S}\varepsilon^{-1/3}$, here N_{α_S} is the dissipation (destruction) rate for half the scalar variance and α_S denotes the temperature or specific humidity respectively ($\alpha_S = T$ or q).

Similarly, the frequency energy spectrum of the temperature (or ecific humidity), $S_T(f)$, in the inertial subrange may be written as (see Eq. 4):

$$S_T(f) = \beta_K (U/2\pi)^{2/3} N_T \varepsilon^{-1/3} f^{-5/3}, \tag{8}$$

where β_K is the Kolmogorov (Obukhov-Corrsin) constant for a passive scalar; a value $\beta_K = 0.8$ (e.g., Kaimal and Finnigan 1994) is used here.

2.2 Monin–Obukhov Similarity Functions for the Structure Parameters

Monin–Obukhov similarity theory (MOST) is the commonly accepted approach for describing near-surface turbulence in the stratified atmospheric boundary layer (ABL). At present, in almost all numerical models (from local and mesoscale to global circulation and climate models), turbulent fluxes are parametrized using MOST or/and a bulk flux algorithm. According to MOST, any properly scaled statistics of turbulence at reference height z are universal functions of a stability parameter $\zeta = z/L$ defined as the ratio of z and the Obukhov length scale, L (Obukhov 1946):

$$\zeta = -\frac{\kappa g z}{T_v} \frac{\overline{w' T_v'}}{u_*^3}, \tag{9}$$

where u_* is the friction velocity, T_v is the virtual temperature, g the acceleration due to gravity, and κ the von Kármán constant. In particularly, nondimensional structure parameters of the longitudinal velocity component, C^2_u, and temperature, C^2_T, can respectively be written as:

$$\varphi_{Cu2}(\zeta) = \frac{C_u^2 z^{2/3}}{u_*^2}, \tag{10}$$

$$\varphi_{CT2}(\zeta) = \frac{C_T^2 z^{2/3}}{T_*^2}, \tag{11}$$

where $T_* = -\overline{w'T'}/u_*$ is the temperature scale (e.g., Kaimal and Finnigan 1994). It is often assumed perfect scalar similarity conditions (Hill 1989) when Monin–Obukhov similarity functions for the structure parameters of temperature (11) and humidity are identical (or at least very similar), i.e., $\varphi_{CT2}(\zeta) = \varphi_{Cq2}(\zeta)$. While this assumption is a useful theoretical starting point, in reality it is not always accurate.

Nondimensional structure parameters of the lateral (v) and vertical (w) velocity components or specific humidity (q), can be written similarly to (10) and (11), respectively. By using relationships $C^2_u \propto \varepsilon^{2/3}$ and $C^2_T \propto N_T \varepsilon^{-1/3}$, the universal function (10) and (11) can be expressed as $\varphi_{cu2} \infty \varphi_\varepsilon^{2/3}$ and $\varphi_{CT2}\ \alpha\ \varphi_{NT} \varphi_\varepsilon^{-1/3}$, where:

$$\varphi_\varepsilon(\zeta) = \frac{\kappa z \varepsilon}{u_*^3}\ , \tag{12}$$

$$\varphi_{NT}(\zeta) = \frac{\kappa z N_T}{u_* T_*^2}\ , \tag{13}$$

are the nondimensional dissipation rate of TKE and the nondimensional dissipation (destruction) rate for half the temperature variance, respectively.

The exact forms of the universal functions (10) and (11) are not predicted by MOST and must be determined from measurements. However, MOST does predict the asymptotic behaviour of these functions under very stable and extremely unstable stratification (free convection regime). In the neutral case ($\equiv$ 0), these functions are constant. In the free-convection asymptotic limit ($\rightarrow -\infty$), the stress becomes insignificant, and the friction velocity, u_*, ceases to be a scaling parameter; that is, $\varphi_{Cu2} \propto |\zeta|^{2/3}$ and $\varphi_{CT2} \propto |\zeta|^{-2/3}$. In the very stable case ($\gg$ 1), stratification inhibits vertical motion and the turbulence no longer significantly communicates with the surface. In this case, MOST predicts that z ceases to be a scaling parameter; that is, various quantities become independent of z (Obukhov 1946; Monin and Obukhov 1954). This limit requires that z cancels in Eqs. 10 and 11 for $\gg$ 1, which leads to relationships $\varphi_{Cu2} \propto \zeta^{2/3}$ and $\varphi_{CT2} \propto \zeta^{2/3}$, respectively. This approach has been termed the "z-less" concept (i.e., height-independent).

In this study we use the following functional forms of (10) and (11) suggested by Kaimal and Finnigan (1994, their Eq. 2.46 and Eq. 2.47) with one exception which will be explained shortly:

$$Cu2(\zeta) = \begin{cases} 4(1 + 0.5|\zeta|)^{2/3}, & \zeta < 0 \\ 4(1 + 5\zeta)^{2/3}, & \zeta \geq 0 \end{cases} \tag{14}$$

$$\varphi_{CT2}(\zeta) = \begin{cases} 5(1 + 6.4|\zeta|)^{-2/3}, & \zeta < 0 \\ 5\left(1 + 3\zeta^{2/3}\right), & \zeta \geq 0 \end{cases} \tag{15}$$

In the original Kaimal-Finnigan's second Eq. 2.47, $\varphi_{CT2} = 5(1 + 3\zeta)$, the exponent "2/3" was "missed" for stable stratification. Here we follow the widely used form $\varphi_{CT2}(\zeta)$ which provides blending between neutral and very stable (z-less) cases for > 0. Now (15) satisfies both MOST theoretical predictions for the free convection and very stable asymptotic limits. Note that the formulations for $\varphi_{Cu2}(\zeta)$ and $\varphi_{CT2}(\zeta)$ suggested by Kaimal and Finnigan (1994) were derived directly from data by Wyngaard et al. (1971). Further discussion on the Monin–Obukhov similarity functions for the structure parameters can be found in Andreas (1988), Moene et al. (2004), Hartogensis and De Bruin (2005), Li et al. (2012), Wood et al. (2013), Braam et al (2014), Kooijmans and Hartogensis (2016), Perelet et al. (2022), and references therein.

Note that (14) and (15) can be affected by self-correlation because the same variables (primarily the friction velocity, u_*) appear both in the definitions of the universal functions (10) and (11) and in the Monin–Obukhov stability parameter (9). Self-correlation (also referred to as fictitious, spurious, built-in correlation) may lead to spurious dependencies that are not associated with real physics (e.g., Hicks 1978; Mahrt et al. 1998b; Andreas and Hicks 2002; Klipp and Mahrt 2004; Lange et al. 2004; Baas et al. 2006; Grachev et al. 2012 and papers surveyed therein). However, the self-correlation can be overcome, for example, by plotting a universal function and/or stability parameter in a "hybrid" representation without u_* (e.g., Grachev et al. 2018a, Fig. 13 and references therein). This method is based on the idea that a combination of any Monin–Obukhov universal functions is itself a universal function. For example, Grachev et al. (2018a) plotted universal function $\varphi_m \varphi_w^{-1}$ versus $= z/L$, where φ_m and $\varphi_w(\zeta)$ are the nondimensional profile of wind speed and the nondimensional standard deviation of vertical velocity component, respectively. "New" universal function $\varphi_m \varphi_w^{-1}$, by definition, is not affected by the self-correlation because this function shares no variables with the MOST stability parameter (9) except a measurement height z (formally u_* here is replaced by σ_w).

In a similar manner, structure parameters can be normalized by appropriate variances rather than u_* and T_*:

$$f\varphi_{C\alpha^2} = \varphi_{C\alpha^2}^{\alpha^{-2}} = \frac{C_{\alpha^2} z^{2/3}}{\sigma_{\alpha^2}}, \quad (16)$$

where α = u , v, w, T, or q. The nondimensional standard deviations of wind speed components in (16) are scaled as:

$$\varphi_{\alpha_V}(\zeta) = \frac{\sigma\alpha_V}{u_*}, \quad (17)$$

here α_V (= u, v, and w) denotes the longitudinal, lateral, and vertical velocity components respectively. Similarly, standard deviations for scalars, air temperature, σ_T, and specific humidity, σ_q, are scaled as:

$$\varphi_T(\zeta) = \frac{\sigma_T}{|T_*|}, \quad (18)$$

and:

$$\varphi_q(\zeta) = \frac{\sigma_q}{|Q_*|}, \quad (19)$$

where $T_* = -\overline{w\prime T\prime}/u_*$ and $Q_* = -\overline{w\prime q\prime}/u_*$ are the temperature and specific humidity scales respectively.

Plots of 'new' nondimensional structure parameters (16) versus the Monin–Obukhov stability parameter (9) are also not affected by the self-correlation. In addition, variance-based scaling for the structure parameters (16) has a number of advantages over the traditional representation (10)-(11), which we will consider in Sect. 4.4.

2.3 Effects of Temperature and Humidity Fluctuations on C_n^2

As discussed by Wyngaard et al. (1978), Hill et al. (1980), Wyngaard and LeMone (1980), Andreas (1988), Fairall (1991), Frederickson et al. (2000), Moene (2003), Moene et al. (2004), Frehlich et al. 2010; Li et al. (2012), Wilson and Fedorovich (2012), Maronga et al. (2013), Wainwright et al. (2015) Wang et al. (2020); Fiorino et al. (2021) and others, turbulent fluctuations in the refractive index of air, n, have contributions from temperature, humidity, and pressure. In addition, n also depends on wavelength of a propagating wave, λ; this is known as dispersion. Fluctuations of air pressure give a negligible contribution to refraction fluctuations (e.g., Hill et al. 1980). Since the refractive index is generally a function of temperature and humidity, the structure parameter for refractive index, C_n^2, can be expressed in terms of temperature and humidity as well, i.e., through the structure parameters of air temperature, C_T^2, specific humidity, C_q^2, and their cross-structure parameter, C_{Tq}:

$$C_n^2 = A^2 C_T^2 + 2ABC_{Tq} + B^2 C_q^2, \quad (20)$$

where coefficients A and B nominally depend on temperature, humidity, pressure, and, λ. Exact forms of $A(T, q, P, \lambda)$ and $B(T, q, P, \lambda)$ can be found in Andreas (1988) and Frederickson et al. (2000). In the current study, the structure parameters C_T^2 and C_q^2 are estimated from sonic anemometers and a high-speed hygrometer based on Eq. 4 with $c_0 = 0.25$ (spectral method) and their measurements discussed below in Sect. 4. Typically, little information is available about the structure parameters of specific humidity, C_q^2, and evaluation of the temperature-humidity cross-correlation structure parameter, C_{Tq}, remains a challenge (Kohsiek 1982; Fairall 1991). A number of studies have shown, that $C_{Tq} = R_{Tq}\sqrt{C_T^2 C_q^2}$, where R_{Tq} is the correlation coefficient between T and q in the inertial sub-range (e.g. Moene 2003; Beyrich et al. 2005). Wyngaard et al. (1978) and Wyngaard and LeMone (1980) showed that C_{Tq} is directly related to the molecular destruction rate of Tq-fluctuations. Perfect correlation or anti- correlation between T and q assumes that $R_{Tq} = \pm 1$ respectively. Although many studies report that values of $|R_{Tq}|$ generally close to one, R_{Tq} can vary widely depending on the conditions (e.g. Kohsiek 1982; Moene 2003; Beyrich et al. 2005; Lüdi et al. 2005). Estimation of C_{Tq} in Eq. 20 from sonic anemometer data using the spectral approach (similar to C_T^2 and C_q^2) requires derivation of the appropriate Tq-cospectra that was not originally part of the CASPER-East and the C-FOG programs.

Although humidity (and pressure) perturbations also contribute to optical turbulence (e.g., Wesely 1976; Andreas 1988; Frederickson et al. 2000; Moene 2003; Moene et al. 2004), in many cases the largest contributor to C_n^2 over land comes from temperature disturbances. Thus, it is common practice to express C_n^2 in terms of C_T^2, assuming that the humidity-related terms are neglected in Eq. 20, i.e., $C_q^2 \approx 0$ and $C_{Tq} \approx 0$. The most popular relation is the well-known Gladstone-Dale (or just Gladstone) relationship (e.g., Tatarski 1961; Moene et al. 2004; Frehlich et al. 2010; Cherubini and Businger 2013; Maronga et al. 2013; Wood et al. 2013; Basu 2015; Fiorino et al. 2021 and references therein):

$$C_n^2 \approx \left(7.93 \times 10^{-5} \frac{P}{T^2}\right)^2 C_T^2, \tag{21}$$

where T and P are mean temperature [K] and pressure [hPa], respectively. Formally, Eq. 21 is valid for dry air and the constant factor 7.93×10^{-5} is derived for wavelength $\lambda = 0.5$ μm (corresponds to the middle of the visible spectrum). However, it can be said that the effects of humidity are included in C_n^2 in the case if C_T^2 in Eq. 21 is derived from a sonic, because a sonic anemometer measures the so-called 'sonic' virtual temperature, $T_S = T(1 + 0.51q)$, which is close to the virtual temperature, $T_v = T(1 + 0.61q)$, (e.g. Kaimal and Finnigan 1994; Ostashev and Wilson 2015), which is equivalent to using $T_S \approx T_v$ instead of the air temperature T in C_T^2, (see also discussion by Wood et al. 2013 and Fiorino et al. 2021).

Equation 21 is often used together with the equation that relates C_T^2 and the mean temperature gradient (Tatarski 1961). But here we do not consider Tatarski's equation and further discussion of relationships of this type can be found in Frehlich et al. (2010), Cherubini and Businger (2013), Maronga et al. (2013, 2014), Basu (2015). Fiorino et al. (2021), Basu and Holtslag (2022) and references therein. In addition, we note that, C_n^2 can be also expressed in terms of the sonic anemometer-derived velocity structure parameter (Fiorino et al. 2021), which we consider further in Sect. 4.

The simplified formula between C_n^2 and C_T^2 (21) is a widely used standard approximation in C_n^2 studies for average atmospheric conditions, however, in some cases (e.g., over oceans or water-saturated soils) C_n^2 is dominated by C_q^2 or at least the effects of humidity cannot be neglected. Assuming perfect scalar similarity conditions (Hill 1989) for the scalar universal functions (11), i.e., $\varphi_{CT2}(\zeta) = \varphi_{Cq2}(\zeta)$ and $|R_{Tq}| = 1$, and using the formula for the square of a sum, Eq. (20) reduces to (cf. Wesely 1976; Moene 2003; Moene et al. 2004):

$$C_n^2 \approx \left(7.93 \times 10^{-5} \frac{P}{T^2}\right)^2 \left(1 + 0.031 \cdot \mathrm{Bo}^{-1}\right)^2 C_T^2, \tag{22}$$

where $\mathrm{Bo} = H_S/H_L$, is Bowen ratio defined as the ratio of sensible heat flux, $H_S = c_p \rho \overline{w'T'}$, to latent heat flux, $H_L = \mathcal{L}_e \rho \overline{w'q'}$. Here, ρ is the mean air density, c_p is the specific heat capacity of air at constant pressure, $\mathcal{L}_e$ is the latent heat of evaporation of water. Equation 22 can be considered as a modification of Eq. 21 corrected for humidity effects. Note that the Bo-correction in (22) also avoids zero or very small values of C_n^2 in the limit $\frac{\partial T}{\partial z} \to 0$ and $C_T^2 \to 0$ because $\left|\mathrm{Bo}^{-1}\right| \to \infty$ in the near-neutral conditions.

2.4 Coastal Boundary Layers

This study mainly analyses and discusses behaviour of the structure parameters C_α^2 in coastal zones. The coastal zone represents the interface between the land and water, the two footprint surfaces having completely different mechanical and thermal properties. The ocean has a relatively smooth surface (compared to land) and a very large heat capacity, whereas dry inland areas are aerodynamically rough in general and have low heat storage capacity. Thus, the drag coefficient, $C_D = (u_*/U)^2$, surface fluxes, as well as the diurnal cycle of surface meteorology and energy fluxes over these different footprints differ considerably (Grachev et al. 2011, 2018a, 2021; Bardoel et al. 2025, and references therein).

Moreover, modelling of turbulent mixing over different footprint surfaces requires different bulk flux schemes. Specifically, the COARE bulk flux algorithm (Fairall et al. 2003) and the SHEBA bulk turbulent flux algorithm (Andreas et al. 2010a, 2010b) are the present state-of-the-art parameterizations of the turbulent fluxes over statistically homogeneous surfaces where an interfacial value of specific humidity can be unambiguously established (e.g., oceans, lakes, ice, snow covered surfaces, or water-saturated soils). Development of simplified bulk algorithms over land is not as straightforward as for over water or snow/ice because for dry and wet bare soils and simple ground-hugging plant canopies the surface is not near saturation. In this case, u_* and H_S can still be estimated using a traditional aerodynamic method for the turbulent flow (similar to the COARE and SHEBA algorithms), whereas estimating H_L requires a different approach, e.g., based on the combination of surface energy budget and aerodynamic transport equations (see Garratt 1992; Foken 2017; Cuxart and Boone 2020; Grachev et al. 2022). Thus, to derive C_α^2 in a coastal zone from Eqs. 14 and 15, the COARE bulk flux algorithm (Fairall et al. 2003) can be used in the case if the upwind flux footprint corresponds to sea surface and a hybrid bulk algorithm (Grachev et al. 2022) for inland footprints.

Coastal surface heterogeneity produces a complex vertical layered structure when turbulent parameters including the fluxes and the structure parameters become functions of the measurement height (e.g., Mahrt et al. 2018, 2021; Ortiz-Suslow et al. 2021) and/or wind direction (i.e., surface footprints). In particular, sharp changes in the surface characteristics due to the sea-land transition in a case of onshore (or offshore) winds leads to the formation of a thin internal boundary layer (IBL) resolved by a tower (Figs. 1 and 2). An overview of various formulations to predict the IBL height as a function of the fetch can be found in Savelyev and Taylor (2005), Bardoel et al. (2025). A sketch of the IBL in Figs. 1 and 2 represents an idealized concept of an equilibrium IBL (Garratt 1990, 1992), although the actual structure of the vertical layers may be more complex. For example, Mahrt et al. (2018)

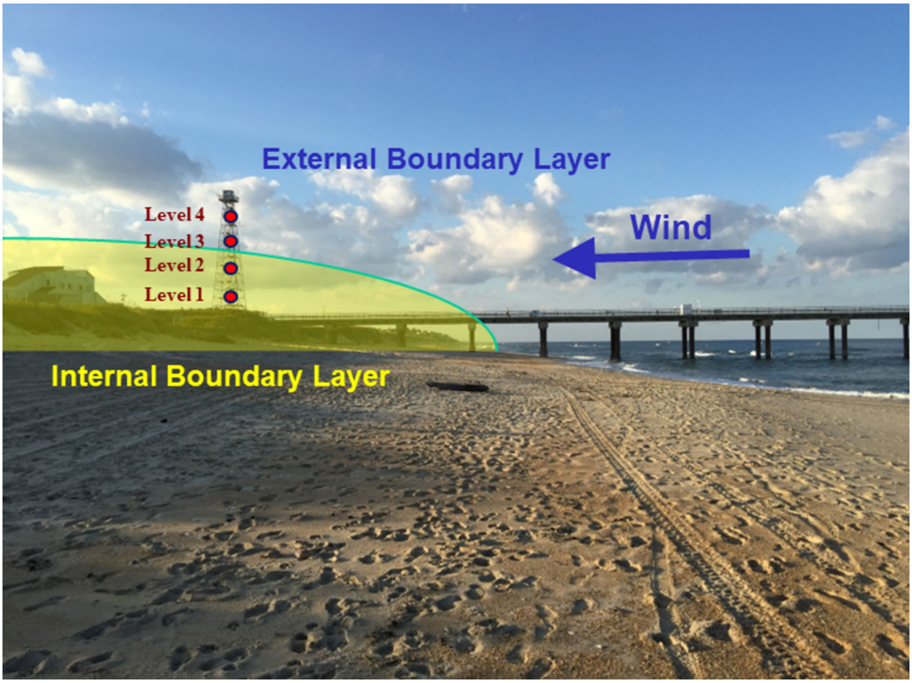

Fig. 1 Sketch of a thin coastal internal boundary layer (IBL) for onshore winds from the Atlantic Ocean during CASPER-East. Note the FRF Video tower (on the left) and a part of the 560-m-long FRF pier. The IBL height is sketched here and located between sonic anemometers at levels 2 and 3 of the FRF Video tower (9.41 and 17.94 m AGL respectively)

considered a three-layer structure, which includes a shallow “new” boundary layer near the surface, an overlying “regional boundary layer”, and the transition layer between these two layers (Mahrt et al. 2018, Fig. 5). Krishnamurthy et al. (2023, Fig. 1b) and Bardoel et al. (2025, Fig. 1a) identified a transition sub-layer above an IBL. In such conditions, the drag coefficient and diurnal variation of the sensible heat flux, among other parameters such as the Bowen ratio, the ratio of sensible heat flux to latent heat flux, and carbon dioxide flux, can be considered as indicators of different surface footprints such as water and land surfaces (coastal IBL markers) discussed further in Sect. 4.1.

Turbulent statistics over heterogeneous surfaces are strongly dependent on an upwind ’flux footprint’ over which the turbulent fluxes and other statistics are sampled (Kljun et al. 2004, 2015; Burba 2013; Leclerc and Foken 2014). In this case, turbulent parameters become functions of the wind direction, and the structure of the air flow can include a front recirculation zone, flow separation, a corner stream zone, and a wake region etc. (e.g., Coceal and Belcher 2004; Klipp 2007; Grachev et al. 2018a and references therein). In addition, the coastal zone is generally complicated by momentum or/and thermal IBLs that appear quite distinctly for onshore and offshore winds. Thus, the wind direction is a main general parameter for interpretation of atmospheric turbulence measurements in such conditions (see Sect. 4.1).

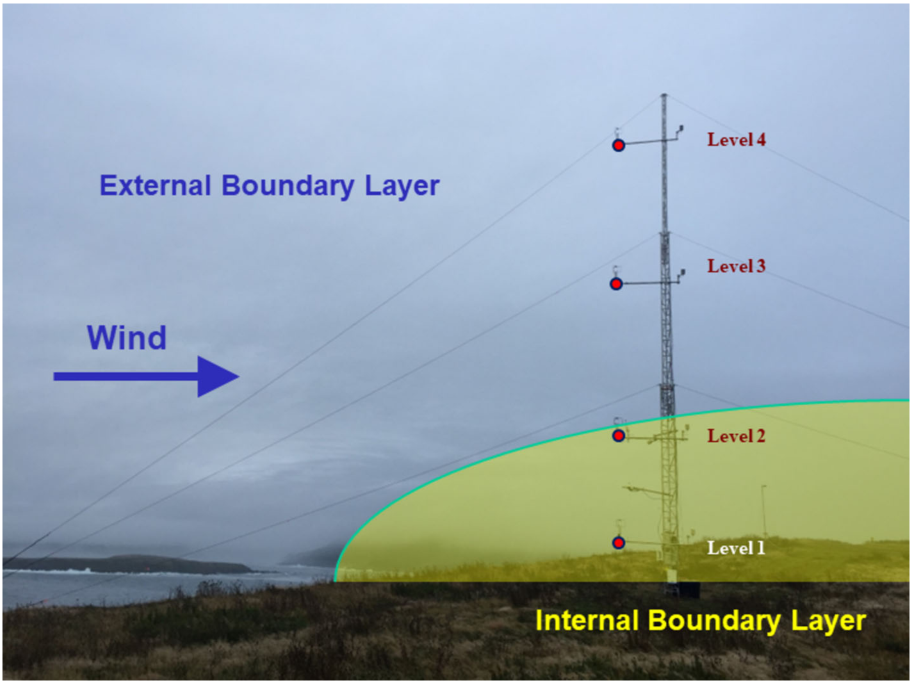

Fig. 2 Sketch of a thin coastal IBL for onshore winds during the C-FOG (Coastal-Fog) field campaign in September–October 2018. Picture also shows the UND tower and instruments located at The Downs site in Ferryland, Newfoundland. The IBL height is sketched here and is located between levels 2 and 3 of the tower (5 and 10 m AGL respectively)

3 Observation Sites and Instrumentations

In this section, we describe two observation sites located on the Atlantic coast (i) near the Duck, Outer Banks, North Carolina (October–November 2015, during the CASPER-East Program) and (ii) near the Ferryland, Newfoundland, Canada (September–October 2018 during the C-FOG or Coastal-Fog field campaign). Instrumentation at each site was used to investigate C_α^2. Various measurements made during CASPER-East and C-FOG have been described previously (see overview papers by Wang et al. 2018 and Fernando et al. 2021 respectively), and below only the relevant information on observation sites, instrumentation, measurements, and data processing are given.

3.1 The CASPER-East Duck Observation Site

CASPER-East took place at the U.S. Army Corps of Engineers Field Research Facility (FRF) located near the town of Duck, North Carolina (north to town of Kitty Hawk, NC); see Wang et al. (2018). The facility situated in the Outer Banks stretches from the Atlantic Ocean to Currituck Sound (Grachev et al. 2018a; Wang et al. 2018). This study focuses on C_α^2, which was not considered by Grachev et al. (2018a). Although we use the same data set, an additional prerequisite (described later in Sect. 4.2) is imposed on the spectral slope in the inertial subrange to derive C_α^2. Note that turbulence measurements in the coastal zone near

Duck NC have been previously reported during the Shoaling Waves Experiment (SHOWEX) in 1997–1999 (e.g., Sun et al. 2001; Vickers et al. 2001) and recently by Potter et al. (2025). The Outer Banks is a 320-km-long chain of narrow barrier islands and peninsulas separating the Atlantic Ocean (to the east) from a system of wide, shallow sounds and the forested, low-lying mainland of North Carolina (to the west). The islands, largely composed of sand, are generally low-lying, with some dunes rising to more than 30 m in height. The Outer Banks has diverse vegetation from beach grasses, sea oats and hardy grasses on the dunes, wax myrtles and bay grasses on the sound side to more protected lush maritime forests with live oaks, pines, and various hardwoods inland.

Turbulence and mean meteorological data were collected at multiple levels on four meteorological flux towers (Grachev et al. 2018a, Figs. 1, 2, 3 and Table 1). The three shore towers, named "Video" (or "Tall"), "Sand Dune Top" (SDT), and "Sand Dune Foot" (SDF) towers, were located at various distances from the shoreline. Oceanfront sand dunes usually reach a height of 3 m or so above the seashore. Fourth tower, called the "FRF Pier tower", was located at the FRF pier. In this study, we use data from the FRF Pier, FRF Video, and one 6-m tall SDT tower. The FRF Pier tower, was located at the end of the 560-m-long FRF

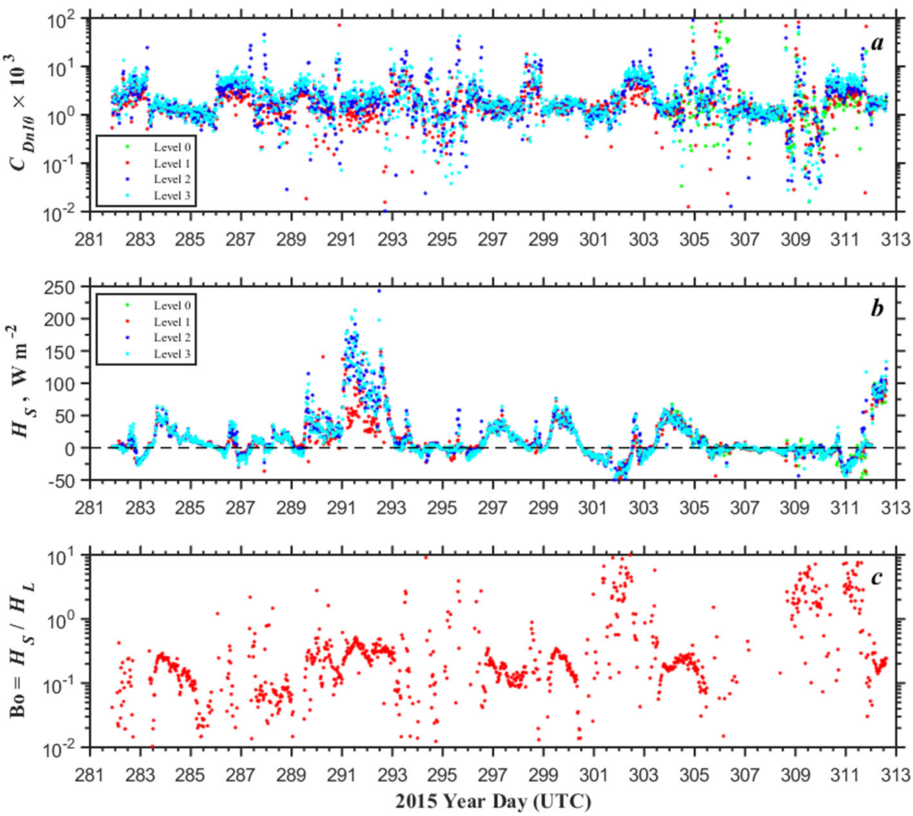

Fig. 3 Time series of coastal IBL indicators: **a** 10-m neutral drag coefficient, C_{Dn10}, **b** sensible heat flux, H_S, and **c** the Bowen ratio, $\mathrm{Bo} = H_S/H_L$, for 2015-year days 281–313 (8 October–9 November 2015) observed during the CASPER-East field campaign over the water at the FRF Pier tower. The data are based on 30-min averaging

pier, i.e., "over water". The FRF pier is oriented along ≈ 72° (in an ENE–WSW direction) and a shoreline is aligned approximately in an NNW–SSE direction (bearing ≈ -18°). Thus, onshore wind directions range from 342° through 162° clockwise. The prevailing winds in Duck NC blow predominantly from the northeast direction due to typical storms that frequent the eastern seaboard.

The FRF Pier tower was instrumented with three levels of sonic anemometers at heights 9.9, 13.22, and 17.91 m above sea level (ASL) and three levels with ’slow’ T/RH probes at 9.80, 13.06, and 17.88 m ASL (Levels 1 to 3 respectively). The LI-7500A (LI-COR Inc.) gas analyser was mounted on the same boom as the sonic anemometer at Level 1 with measurement height 9.9 m ASL (Grachev et al. 2018a, Fig. 3a). The LI-COR made direct measurements of water vapor (latent heat) turbulent fluxes and variables for relevant turbulent statistics. An additional sonic anemometer was installed on October 30 at a measurement height of 7.47 m ASL, i.e., below the pier deck ("Level 0"). On the "FRF Video" tower, the sonic anemometers and the ’slow’ T/RH probes were placed at four levels (Levels 1 to 4). Turbulent data at this tower were collected continuously at 5.11, 9.41, 17.94, and 26.48 m above ground level (AGL) whereas air temperature and humidity ’slow’ data were collected at 4.66, 8.93, 17.46, and 26.0 m AGL respectively. The Video tower base ("ground level" for this tower) is 5 m ASL. The SDT tower had sonic anemometers (2.04, 4.70, 6.16 m AGL), one LI-7500A at level 1, and two T/RH measurements at 1.93 and 6.0 m AGL.

All sonics used were three-axis R.M. Young (Model 81,000) sampled at 20 Hz whereas slow response temperature and relative humidity (T/RH) probes and air pressure sensors were sampled at 1 Hz. The FRF Pier tower was also instrumented with a LI-7500A (20 Hz). The mean wind speed and direction were derived from the sonic anemometers, with rotation of the anemometer axes to place the measured wind components in a streamline coordinate system based on 30-min averaged 20-Hz raw data. We used the most common method, which is a double rotation of the anemometer coordinate system, to compute the longitudinal, lateral, and vertical velocity components (Kaimal and Finnigan 1994, Sect. 6.6). The measurements of air temperature and relative humidity at several levels provided by T/RH probes were used to evaluate the vertical temperature and humidity gradients based on 30-min averaged 1-Hz raw data. Turbulent covariance and variance values were derived from sonic data through frequency integration of the appropriate cospectra and spectra computed from 27.31-min data blocks (corresponding to 2^{15} data points) from the original 30-min data files. The dissipation rate of TKE and destruction rate for half the temperature (humidity) variance in the current study were estimated as in Grachev et al. (2015). Data-quality control screening based on objective and subjective methods (including restrictions on skewness and kurtosis) has been applied to the original flux data to remove spurious or low-quality records. Details of data processing, accuracy, calibration, and data-quality criteria can be found in Grachev et al. (2011, 2015, 2018a, 2018b, 2021).

3.2 The C-FOG Ferryland Observation Site

Bardoel et al. (2021), Dorman et al. (2021), Fernando et al. (2021), Grachev et al. (2021), and Perelet et al. (2021) describe the C-FOG program and the Ferryland observation site, measurements, data processing, data accuracy, and instrument calibration in detail. Here we provide some relevant information about the surface meteorology and turbulence data collected at a supersite located near a small town called Ferryland (in the Island of Newfoundland) during the C-FOG field campaign.

The town of Ferryland is located approximately 80 kms south of St. John's on the south-eastern coast of the Avalon Peninsula and is exposed to the Northwest Atlantic where extensive fog development is frequently observed along the coast of Newfoundland (Dorman et al. 2017). The topography of the area is complex with high rock cliffs, islands, tombolo, rocky shorelines, valleys, and other features including inlets and bays. The study area is located on a long peninsula just east of Ferryland and the location is dubbed "The Downs". The Downs can be thought of as a sloping land covered in grass and largely treeless, and its seascapes range from cobbled and sandy beaches to sheer rocky cliffs. The centrepiece of the University of Notre Dame (UND) turbulence program was a 16.2-m tower erected at The Downs (47°01′17.1"N and 52°52′19.5"W) to examine air-sea/land coupling in the coastal zone with and without fog (Grachev et al. 2021). Surface meteorology, turbulent fluxes of momentum , sensible and latent heat and and other relevant turbulent statistics were measured continuously on the tower at four levels, at 2, 5, 10 and 15 m AGL (see also Fernando et al. 2021, Table 2 for measurement instruments deployed during C-FOG for The Downs site). The UND tower base ("ground level" for this tower) is approximately 32 m ASL. Each measurement level was instrumented with identical fast response three-axis sonic anemometers, sampling the wind velocity and sonic temperature at 20 Hz (R.M. Young Model 81,000) and Rotronics HC2S3 temperature and relative humidity probes (T/RH, sampling frequency = 1 Hz). The HC2S3 probes were housed in ventilated radiation shields. A fast-response (20 Hz) open path infrared gas analyser (LI-7500A, LI-COR Inc.) was collocated with a sonic anemometer at 5-m height for direct measurements of water vapor and carbon dioxide turbulent fluxes and other relevant H_2O and CO_2 turbulent statistics. In addition, an optical sensor Väisälä Present Weather Detector, PWD22, mounted on a boom at an intermediate level between 2-m and 5-m instrument levels, and is used for direct measurements of visibility, precipitation intensity, and precipitation type. Measurements were collected by a data-logger (Campbell CR3000) and successively parsed into 15-min data files. For the C-FOG study we use a 15-min averaging time instead of the conventional 30-min benchmark. A shorter interval can provide more detail on rapid fog changes in this study. Other details regarding the observation site, the instrumentation, and the data can be found in Bardoel et al. (2021), Dorman et al. (2021), Fernando et al. (2021), Grachev et al. (2021), and Perelet et al. (2021).

4 Measurements of the Structure Parameters at Coastal Zones

In this section, we analyse observations from two sites located on the Atlantic coast (near the town of Duck, North Carolina and near the town of Ferryland, Newfoundland, Canada) to investigate the horizontal and vertical structure of the structure parameters C_α^2 in a coastal internal boundary layer (IBL).

4.1 Turbulent Indicators (Markers) of a Coastal IBL

As discussed in Sect. 2.4, behaviour of various turbulent statistics in coastal zones (including the structure parameters C_α^2) are strongly dependent on an upwind flux footprint. In this section, we consider different indicators for different surface footprints in more detail for subsequent analysis of C_α^2. The wind direction is a main general parameter for interpretation of atmospheric turbulence measurements in such conditions. The time series of the wind direction observed during the CASPER-East field campaign can be found in Grachev et al. (2018a, Fig. 4b). The CASPER-East data presented in this study were collected during 8

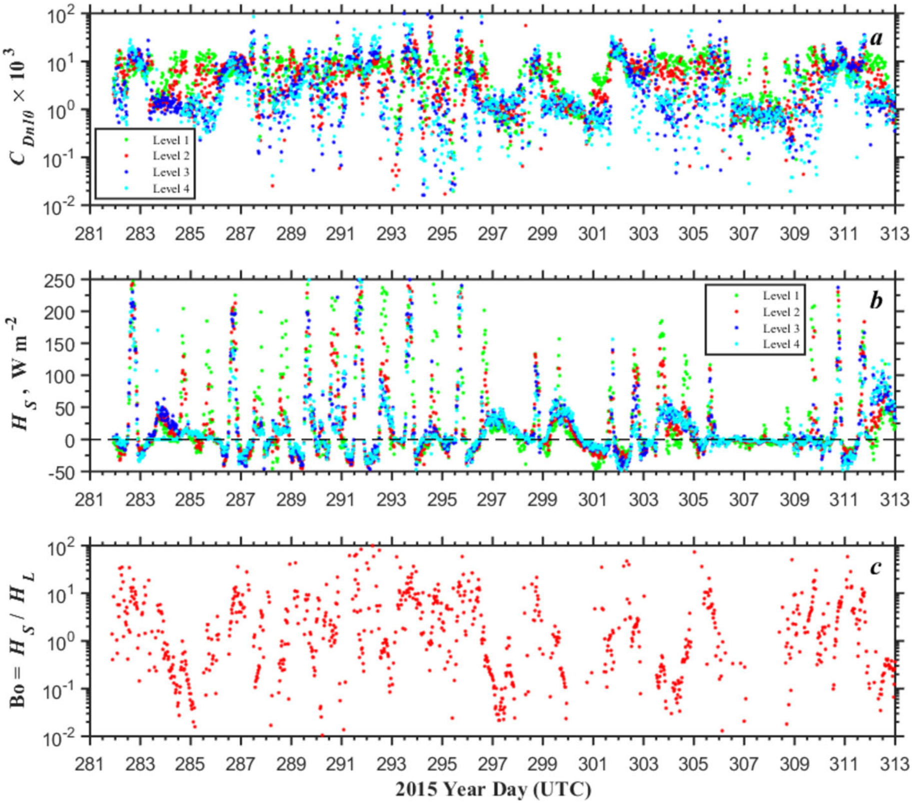

Fig. 4 Time series of coastal IBL indicators: **a** 10-m neutral drag coefficient, C_{Dn10}, **b** sensible heat flux, H_S, and **c** the Bowen ratio, Bo $= H_S/H_L$, for 2015-year days 281–313 (8 October–9 November 2015) observed during the CASPER-East field campaign over land at the FRF Video tower (panels *a*, *b*, and *c*) and the SDT tower (panel *d*). The data are based on 30-min averaging

October through 9 November 2015, corresponding to the year day (YD) from 281 through 313 with respect to January 1, 2015 UTC. Similar wind direction plots from the UND tower located at The Downs measurement site in Ferryland during the C-FOG field campaign from 1 September through 6 October 2018 (YD 244–279 with respect to January 1, 2018 UTC) are shown in Grachev et al. (2021, Fig. 3b).

As mentioned, the drag coefficient allows the determination of whether the upwind flux footprint corresponds to a relatively smooth sea surface or aerodynamically rough dry inland areas. To compare measurements taken at different levels above the surface for different stratifications, the drag coefficient adjusted to a standard height of 10 m and neutral conditions, C_{Dn10}, is widely used in the boundary layer studies (e.g., Fairall et al. 2003; Andreas et al. 2012; Vickers et al. 2013 and where the definition of C_{Dn10} can be also found). Our observations show that the average drag coefficient C_{Dn10} over land is generally larger than over the sea surface due to the change in aerodynamic properties of the surface. For onshore winds, the vertical profiles of C_{Dn10} measured at the coastal tower allows us to determine the position of the coastal IBL. Time series of the 10-m neutral drag coefficient are presented in Figs. 3, 4 and 5 (panel a). According to our data, the magnitude of C_{Dn10} observed over

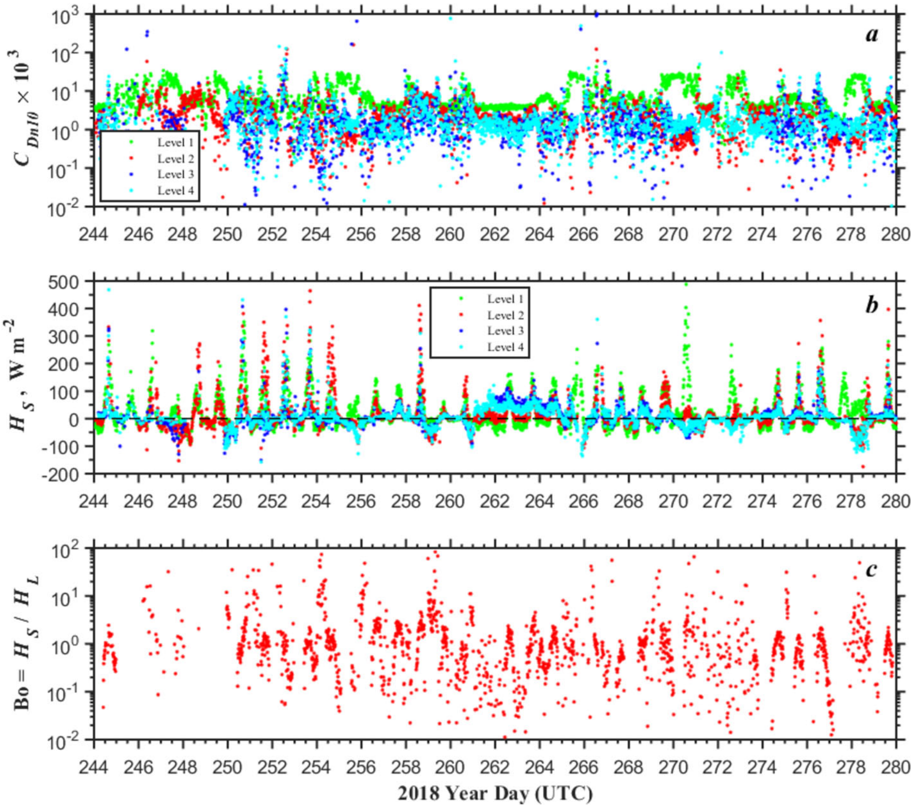

Fig. 5 Time series of coastal IBL indicators: **a** 10-m neutral drag coefficient, C_{Dn10}, **b** sensible heat flux, H_S, and **c** the Bowen ratio, Bo $= H_S/H_L$, for 2018-year days from 244 through 279 (from 1 September through 6 October 2018) observed at four levels of the UND tower located at The Downs measurement site during the C-FOG field campaign. The data are based on 15-min averaging

water at the FRF Pier tower (Fig. 3a) during CASPER-East can be an order of magnitude less than measured over land at the FRF Video tower during CASPER-East (Fig. 4a) and at the UND Ferryland/Downs tower during C-FOG (Fig. 5a); $C_{Dn10} \sim 10^{-3}$ vs. $C_{Dn10} \sim 10^{-2}$ respectively.

Figure 4a shows notable cases of a thin convective IBL resolved by the FRF Video tower for onshore winds in the direction sectors from the north to the north-east during the YD 283–286; 299–300; 303–305, among other cases. The sharp vertical change in C_{Dn10} may be attributed to the fact that sonic anemometers at levels 1 and 2 are located within the IBL which is associated with a rough inland footprint, whereas the upper sonic anemometers (levels 3 and 4) belong to the external boundary layer which is associated with relatively smooth sea-surface footprints. In this case the IBL height is located between sonic anemometers at levels 2 and 3 (9.41 and 17.94 m AGL respectively) as sketched in Fig. 1. Similar behaviour of C_{Dn10} is associated with the presence of an IBL and can be found in the time series of the C-FOG field campaign (see sketch in Fig. 2). According to Fig. 5a, values of C_{Dn10} measured by two upper sonic anemometers (levels 3 and 4) are located outside the IBL and correspond in general to sea-surface footprints ($C_{Dn10} \sim 10^{-3}$), whereas C_{Dn10} observed at the lower level 1, is located within the IBL and associated with the rough inland footprints (level 2 shows mixed behaviour). The high values of $C_{Dn10} \sim 10^{-1}$ which are observed at level 1 during the YD 247, 265.5, 270, 278 among other cases (Fig. 5a) for onshore are likely due to the influence of individual upwind obstacles such as a sharp-edged coastal cliff (see Grachev et al. 2021). Additional examples of C_{Dn10} behaviour over different footprint surfaces in the Houston/Galveston region and the nearby coastal zone can be found in Grachev et al (2011, Figs. 11a and 14a).

While variations of C_{Dn10} are associated with mechanical properties of the underlying surfaces, variations in the sensible heat flux, H_S, are due to the change in the thermal properties of the footprint surfaces (e.g., heat capacity and thermal conductivity). In other words, C_{Dn10} and H_S (among others) can be considered as aerodynamic and thermal markers of a coastal IBL respectively. These IBL markers are associated with two distinct IBLs: the aerodynamic IBL and the thermal IBL, which often form simultaneously in coastal zones, resulting in a complex, inhomogeneous atmospheric boundary layer. Time series of H_S measured over the water (FRF Pier tower) and over land (FRF Video tower) during CASPER-East are shown in Fig. 3c and Fig. 4c, respectively. Similar time series of H_S observed at the UND Ferryland/Downs tower during C-FOG are presented in Fig. 5b. According to Figs. 3, 4 and 5 (panel b), there is a pronounced diurnal cycle evident in H_S observed for rough inland footprints (mainly on levels 1 and 2 Figs. 4, 5), whereas for H_S measured over sea surface (Fig. 3b) such a cycle is only marginally observed (see also discussion in Grachev et al. 2018a, 2021).

The Bowen ratio, $\mathrm{Bo} = H_S/H_L$, can be considered as another marker of a coastal IBL. Generally, the latent heat flux, H_L, over water bodies is higher than the sensible heat flux, H_S, and hence $|\mathrm{Bo}| < 1$. Over dry inland regions, it is vice versa, $|\mathrm{Bo}| > 1$. Typically, the Bowen ratio ranges from about 0.1 over tropical oceans, through 0.5–1 over wet soils/grassland to 5.0 over semiarid regions, and 10 over deserts. In some sense, the Bowen ratio indicates how wet a flux footprint is. Examples of H_S and H_L over wet and/or water-saturated soils and over dry bare or lightly vegetated soil surfaces can be found in Grachev et al. (2020, Figs. 6, 8a, and 8b) and Grachev et al. (2022, Figs. 4 and 6). Time series of the Bo are shown in Figs. 3, 4 and 5 (panel c). The magnitude of Bo over water at the FRF Pier tower (Fig. 3c) is generally less than that over land at the SDT tower (Fig. 4c) and at the UND Ferryland/Downs tower (Fig. 5c).

Although we have considered the main indicators of a coastal IBL here (C_{Dn10}, H_S, and Bo), other parameters can also provide useful information. For example, air temperature and relative humidity (T/RH) have a pronounced diurnal cycle over land similar to H_S, whereas over water at the FRF Pier tower such a cycle in T/RH data is practically not observed.

To summarize, we note that a coastal IBL in a case of onshore winds (Figs. 1 and 2) is associated with encountering aerodynamically rough dry inland footprint areas and hence with high $C_{Dn10} \sim 10^{-2}$–10^{-1}, strong diurnal variations of H_S and T/RH, and $|\mathrm{Bo}| > 1$ among other things, while the external boundary layer corresponds in general to relatively smooth sea-surface footprints and, therefore, $C_{Dn10} \sim 10^{-3}$, $|\mathrm{Bo}| < 1$, and the absence of strong diurnal variations of H_S and T/RH due to high heat capacity and thermal conductivity of the ocean. Note that coastal IBLs for onshore winds (sketched in Figs. 1 and 2) and related analysis of the IBL indicators can be used for testing of potential IBL height predictions (e.g., Garratt 1990, 1992; Savelyev and Taylor 2001, 2005; Fairall et al. 2006; Krishnamurthy et al. 2023; Bardoel et al. 2025 among others) and footprint models (e.g., Horst and Weil 1992, 1994; Kormann and Meixner 2001; Kljun et al. 2004, 2015; Burba 2013; Wilson 2015). It

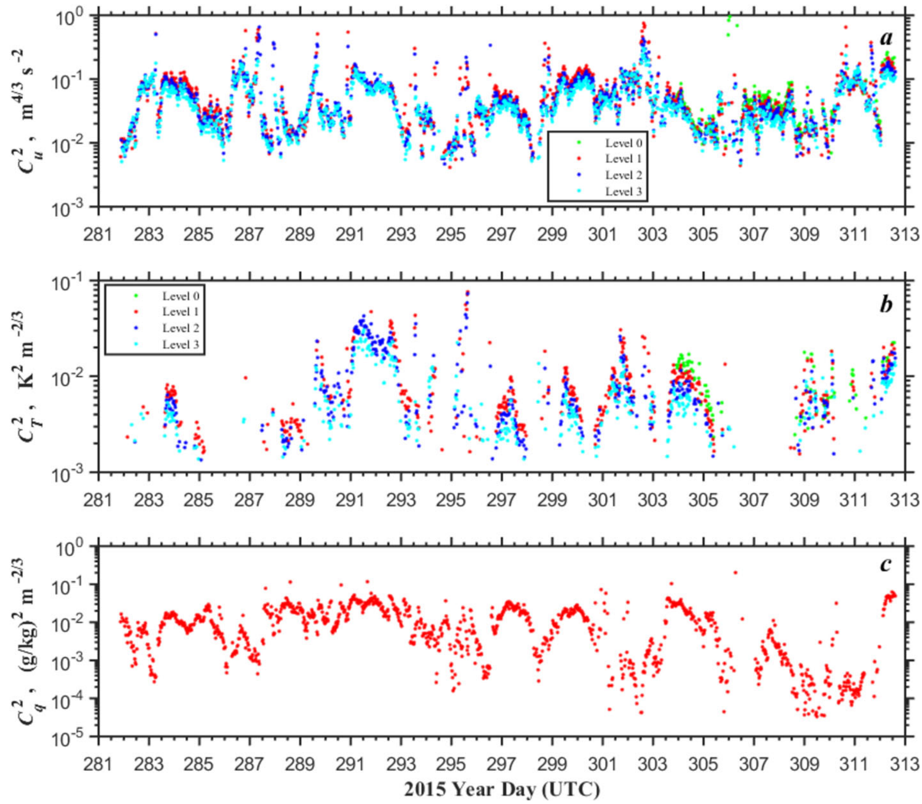

Fig. 6 Time series of the structure parameters of **a** the longitudinal velocity component, C_u^2, **b** the temperature, C_T^2, and **c** the specific humidity, C_q^2, for 2015-year days 281–313 (8 October–9 November 2015) observed during the CASPER-East field campaign over the water at the FRF Pier tower. The data are based on 30-min averaging

should be also noted that this study mainly focuses on the behaviour of C_α^2 in coastal zones and the IBL concept considered here is only an analytical tool and not a research goal.

4.2 Temporal and Directional Variability of the Structure Parameters over Different Surface Footprints

Here, we consider the time series of dimensional structure parameters measured at different towers and different observation levels at the coastal zones described in the Sect. 3. The time-series data allow us to analyse diurnal variations and compare the structure parameters over different footprints, including relatively smooth sea surface conditions and aerodynamically rough dry inland areas under stable and unstable conditions measured over the same time periods.

Figures 6 and7 show the 30-min averaged structure parameters C_α^2 observed during the CASPER-East field campaign over the water (FRF Pier tower) and over land (FRF Video and SDT towers) respectively. Appropriate time series of wind speed, wind direction, air

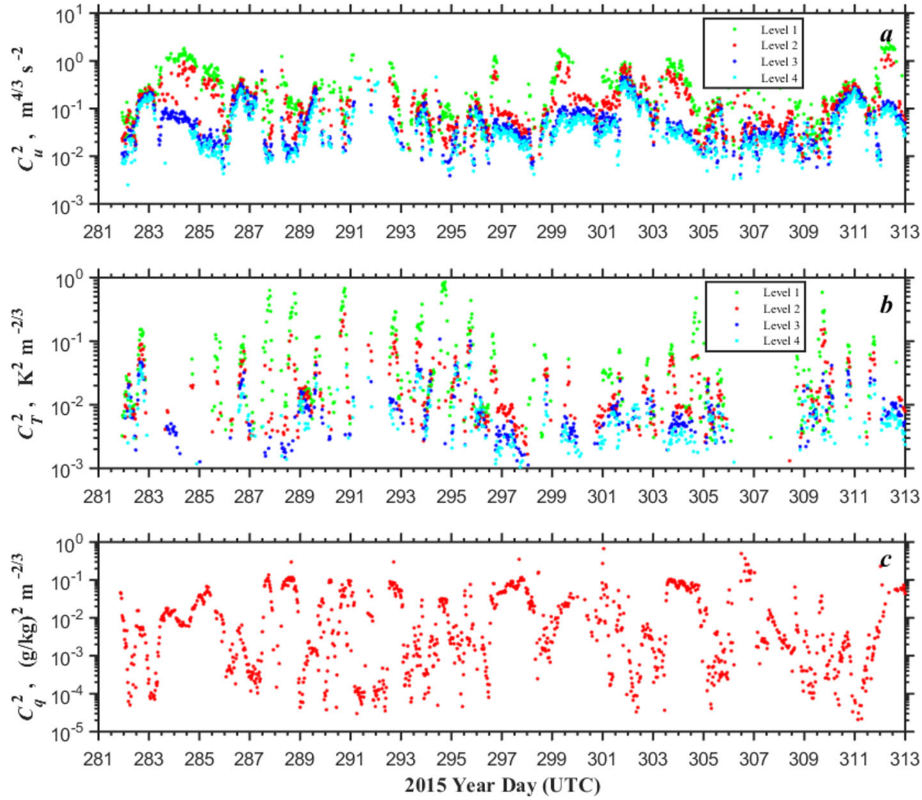

Fig. 7 Time series of the structure parameters of **a** the longitudinal velocity component, C_u^2, **b** the temperature, C_T^2, and **c** the specific humidity, C_q^2, for 2015-year days 281–313 (8 October–9 November 2015) observed during the CASPER-East field campaign over land at the FRF Video tower (panels *a*, *b*, and *c*) and the SDT tower (panel *d*). The data are based on 30-min averaging

temperature, relative humidity, friction velocity, u_*, sensible heat flux, H_S, latent heat flux, H_L, the drag coefficient, the Bowen ratio, and the Monin–Obukhov stability parameter, $\zeta = z/L$, observed at the FRF Pier, FRF Video, and SDT towers for this time period can be found in Grachev et al. (2018a, Figs. 4, 5 and 6) and Figs. 3, 4.

Similar plots of 15-min-averaged C_α^2 values measured in the C-FOG field campaign are shown in Fig. 8. The time series data from the C-FOG experiment shown in Fig. 8 provides additional evidence of the temporal behaviour of the structure parameters at a coastal zone over different footprint surfaces for both stable and unstable conditions. Plots of the 15-min-averaged surface fluxes, basic meteorological variables, and other relevant variables as observed during the entire C-FOG field campaign can be found in Grachev et al. (2021, Figs. 3, 4 and 5) and Fig. 5.

Because our estimates of structure parameters C_α^2 are based on Eq. 4, data without the Richardson-Kolmogorov cascade should be filtered out. In the current study, the following prerequisite is imposed on the data: the data points where the spectral slope in the inertial subrange (in the frequency domain ≈ 0.9–2.7 Hz) deviated more than 20% of the theoretical -5/3 slope were excluded from the analysis (cf. Hartogensis and De Bruin 2005, where ±

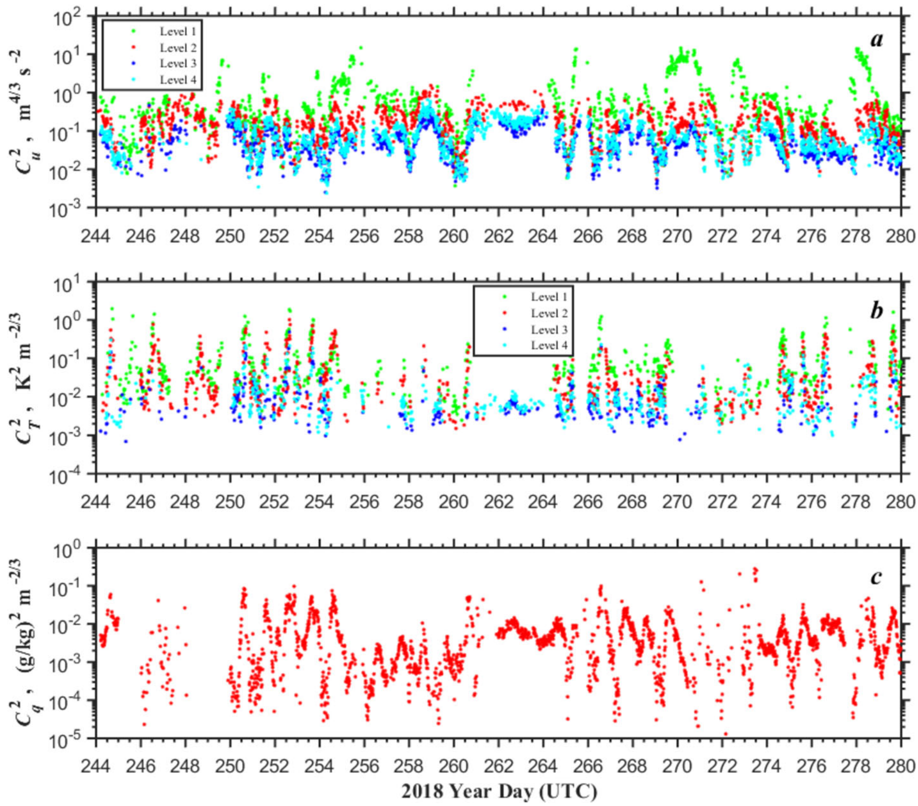

Fig. 8 Time series of the structure parameters of **a** the longitudinal velocity component, C_u^2, **b** the temperature, C_T^2, and **c** the specific humidity, C_q^2, for 2018-year days from 244 through 279 (from 1 September through 6 October 2018) observed at four levels of the UND tower located at The Downs measurement site in Ferryland, Newfoundland during the C-FOG field campaign. The data are based on 15-min averaging

20% was also used). According to our data, the frequency domain ≈ 0.9–2.7 Hz is certainly within the inertial subrange. Estimates of the fraction of the total dataset that passed through the QC screening, for example, for C-FOG data can be found in Grachev et al. (2021, p.402).

According to our data, the structure parameters of a velocity component $C^2_{\alpha_V}$ ($\alpha_V = u, v, w$) collected for the same time periods are highly correlated with one another (see also Eq. 7). The structure parameters of the lateral velocity component, C_v^2, is not shown here because its behaviour is very similar to the longitudinal and vertical velocity components, C_u^2 and C_w^2. Although the structure parameters in Figs. 6 and 7 at different instrument levels at both the FRF Pier and FRF Video towers observed for the same time periods are qualitatively very similar, there are noticeable differences between these two locations that are associated with the different aerodynamic properties of the underlying surface. According to Figs. 6a and. 7a, the amplitude of the 30-min averaged values of C_u^2 at the FRF Pier tower is generally less than that at the FRF Video tower. This may be attributed to the relatively smoother ocean surface as compared to land. The difference is most clearly visible in C_u^2 at the FRF Video tower measured at different levels for the same time periods. This sharp change in the surface characteristics due to the sea-land transition for onshore winds leads to the formation of a thin IBL resolved by the tower as discussed in Sect. 4.1.

The FRF Video-tower data in Fig. 7a show the sharp vertical change in C_u^2 for onshore wind during the YD 283–286; 299–300; 303–305, among other cases. Lower C_u^2 measured by two sonic anemometers at levels 3 and 4 correspond to sea surface footprints whereas the higher values of C_u^2 observed at the two lower levels, 1 and 2 are associated with the rough inland footprints. This sharp vertical change in C_u^2 is caused by a decoupled boundary layer system, and in this case the IBL height is located between sonic anemometers at levels 2 and 3 (see Fig. 1). According to Fig. 7a, the average C_u^2 over land footprints can be an order of magnitude larger than over the sea surface due to the change in surface aerodynamic properties. Similar behaviour of C_u^2 can be found in the time series for the C-FOG campaign (Fig. 8a). For example, C_u^2 measured at Level 1 for ≈ YD 269–271 increased dramatically, as much as an order of magnitude larger than those measured at Levels 2–4 (Fig. 8a).

The two bottom panels in Figs. 6, 7 and 8 show the structure parameters for scalars, temperature, C_T^2, and specific humidity, C_q^2, respectively. According to these plots, the magnitude of C_T^2 and C_q^2 observed over water (FRF Pier tower, Fig. 6b, c) is generally less than that over land during CASPER-East (FRF Video tower, Fig. 7b, c) and C-FOG (Fig. 8b, c). This may be due to the more thermally homogeneous ocean surface compared to the land terrain (i.e., thermal roughness is less for the water surface). Furthermore, there is a pronounced diurnal cycle in C_T^2 which is observed over land (corresponding to inland footprints) during CASPER-East (FRF Video tower, Fig. 7b) and C-FOG (Fig. 8b, e, g, for YD 250–255). There is also a pronounced diurnal cycle of C_q^2 measured in C-FOG (Fig. 8c). Nevertheless, the diurnal cycle for C_T^2 and C_q^2 is weak for relatively smooth sea-surface footprint. This corresponds to the observations in the CASPER-East field campaign at the FRF Pier tower (Fig. 6b, c) and the SDT tower (Fig. 7c). Similar behaviour of C_T^2 and C_q^2 was also observed in C-FOG during YD 261–265 (Fig. 8b, c). In addition, according to our measurements, the structure parameters C_α^2 (in dimensional forms) decrease with increasing measurement height. This is especially clear from Fig. 6 over the sea, when it can be assumed that for all sensors at the tower footprint surfaces (sea roughness and temperature) are approximately the same (i.e., the prerequisite "ceteris paribus" is met).

In addition to time series of the structure parameters C_α^2 (Figs. 6, 7 and 8), their dependence on wind direction can also shed light on coastal variability of C_α^2. Figure 9 shows the structure parameters C_α^2 ($\alpha = u, T$, and q) as a function of true wind direction measured at the FRF Video tower (Fig. 9a, b) and the SDT tower (Fig. 9c) as the most illustrative example. According to Fig. 9, the structure parameters are very sensitive to the wind direction, because a change in wind direction results in sampling of very different upwind surface characteristics. Relatively small values of $C_u^2 \sim 10^{-2}$–10^{-1} m$^{4/3}$ s^{-2} and $C_T^2 \sim 10^{-3}$–10^{-2} K^{2}m$^{-2/3}$ measured by two upper sonic anemometers (levels 3 and 4) were predominantly observed during onshore wind directions, particularly in the sector between 342° through 72° (the prevailing wind sector) correspond to sea surface footprints whereas C_u^2 and C_T^2 observed at two lower levels 1 and 2 are associated with the rough inland footprints the influence of individual obstacles such as a sharp-edged coastal cliff (Fig. 9a, b respectively). According to our data presented in Fig. 9, values of C_u^2 and C_T^2, are generally higher for offshore than for onshore winds (this is especially noticeable for levels 3 and 4). The C_q^2 values, on the

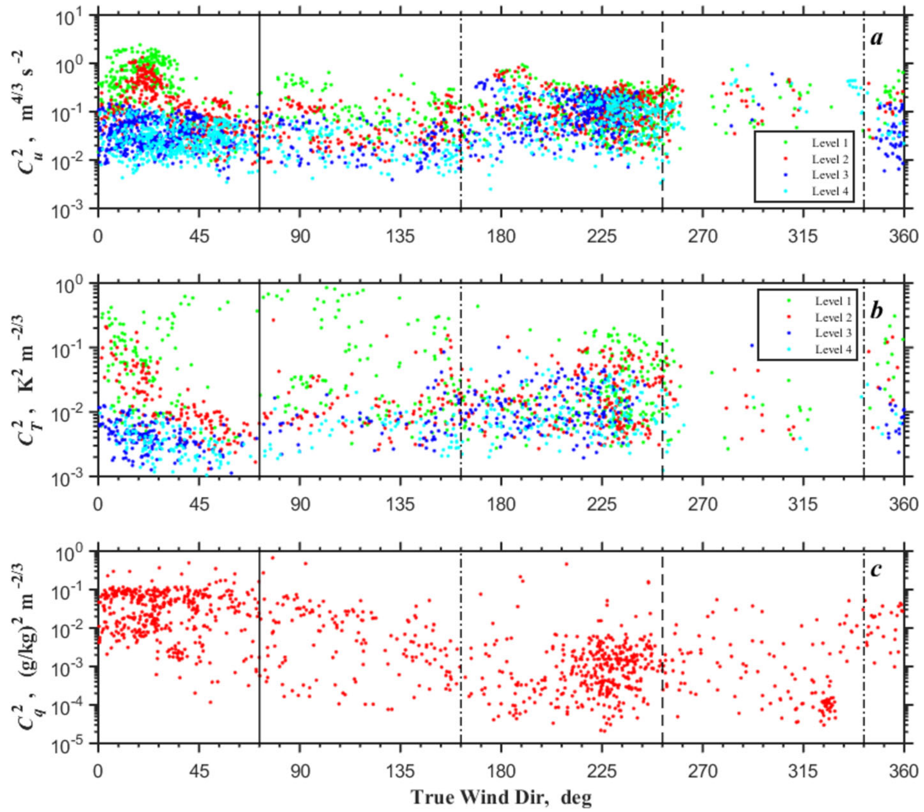

Fig. 9 Individual 30-min-averaged data of the structure parameters of **a** the longitudinal velocity component, C_u^2, **b** the temperature, C_T^2, and **c** the specific humidity, C_q^2, plotted versus the true wind direction for 2015-year days 281–313 (8 October–9 November 2015) observed during the CASPER-East field campaign over land at the FRF Video tower (panels *a* and *b*) and the SDT tower (panel *c*). The FRF pier is oriented along ≈ 72° in an ENE–WSW direction (solid vertical lines), perpendicular to the shoreline which is aligned approximately in NNW–SSE direction. Thus, onshore wind directions range from 342° through 162° clockwise (dash-dotted vertical lines)

contrary, are higher for the onshore than for the offshore winds (Fig. 9c), i.e. higher for sea-surface footprints than for dry inland footprints (e.g., compare C_q^2 values in the direction sector between 342° through 72° with C_q^2 values in the sector from ≈ 180° to ≈ 270°).

Thus, although the CASPER-East and C-FOG observational sites represent different coastal environments and landforms, the temporal variability of the structure parameters is qualitatively similar when they are measured at the towers erected over land (FRF Video tower in Duck NC and the UND tower in Ferryland, Fig. 7 and Fig. 8, respectively). Note also, there is general consistency between our measurements of C_T^2 using a sonic anemometer/thermometer and measurements of C_T^2 by other authors including direct measurements between two points and estimates by scintillometers (e.g., Gur'yanov et al. 1987; Beyrich et al. 2005; Wood et al. 2013; Aristidi et al. 2015). At the same time, the time series of the structure parameters measured at both towers deployed on land (Fig. 7 and Fig. 8) differ from those obtained over the sea surface (Fig. 6). Note that according to Eq. (22), the value $C_T^2 = 10^{-2}$ K^{2}m$^{-2/3}$ in these plots corresponds to $C_n^2 \approx 7.9$ m10$^{-15-2/3}$ and $C_T^2 = 10^{-1}$ K^{2}m$^{-2/3}$ corresponds to $C_n^2 \approx 7.9$ m10$^{-14-2/3}$ (for $T = 300$ K, $P = 1013$ hPa, $\lambda = 0.5$ µm, and dry air).

In summary, the lower values of the dimensional structure parameters are associated with higher altitudes, smooth surfaces (e.g., over water) and stable stratifications (nocturnal boundary layer); that is, for those cases where the level of turbulence is lower.

4.3 Verification of Monin–Obukhov Similarity for the Structure Parameters

The CASPER-East and C-FOG datasets allow us to evaluate MOST predictions for the structure parameters under conditions that violate the horizontal homogeneity assumptions underlying MOST, such as coastal zones. Specifically, we compare data with relationships (14) and (15) suggested by Kaimal and Finnigan (1994).

Figure 10 shows the normalized (according to (10) and (11)) bin-averaged dependencies of the structure parameters of the longitudinal velocity component C_u^2 (panels a and b), the vertical velocity component C_w^2 (panels c and d), the air temperature C_T^2 (panels e and f), and the specific humidity C_q^2 (panels g and h) for CASPER-East over the water at the FRF Pier tower. Similar plots for CASPER-East over land at the FRF Video tower (panels a-f) and the SDT tower (panels g and h) are shown in Fig. 11, and similar plots for the UND tower at Downs (Ferryland) during C-FOG is shown in Fig. 12. The data in Figs. 10, 11 and 12 is plotted in log–log coordinates versus the local stability parameter, $\zeta = z/L$ evaluated at each observational level (local scaling). The left panels in Figs. 10, 11 and 12 (panels a, c, e, and g) present unstable ($\zeta < 0$) conditions, whereas the right panels (b, d, f, and h) are for stable ($\zeta > 0$) conditions. The individual half-hour (Fig. 10 and Fig. 11) and 15-min-averaged (Fig. 12) data of C_α^2 for all measurement levels are also shown in Figs. 10, 11 and 12 as background yellow dot-symbols. These data-points give an estimate of the available data at all levels and the typical scatter of the data.

Figure 12 for the C-FOG data shows non-fog conditions only. Similar to the Grachev et al. (2021) study, here we have imposed the visibility threshold to 6 km to separate turbulence data into fog and no fog categories. In this study as well as in Grachev et al. (2021), by fog-free conditions (i.e., clear sky days with high visibility) we mean that the visibility measured by the PWD22 was greater than 6 km, based on the suggestion by Dorman et al. (2021).

According to Figs. 10–12 (panels a-d), the nondimensional structure parameters of the velocity components measured in the coastal zone, on the average, follow MOST local scaling for both stable (> 0) and unstable (< 0) stratifications. Furthermore, the data points for different measurement levels collected at different towers collapse fairly well into a universal curve, especially over the water at the FRF Pier tower during the CASPER-East field campaign (Fig. 10 panels a-d). In general, our observations over land (Figs. 11 and 12) show larger scatter of individual and averaged data-points for the nondimensional structure parameters as compared with data collected over the water (Fig. 10), possibly due to complexity of coastal landforms of the Outer Banks (North Carolina) and Ferryland (Newfoundland) compared to the ocean surface. Thus, Figs. 10, 11 and 12 demonstrate similarities and differences in behaviour of C_α^2 over different footprint surfaces in coastal zones.

The dimensionless temperature structure parameter C_T^2 for near-neutral conditions $|\zeta| \to 0$ is ambiguous (Figs. 10, 11 and 12, panels e and f) because the temperature scale T_* is

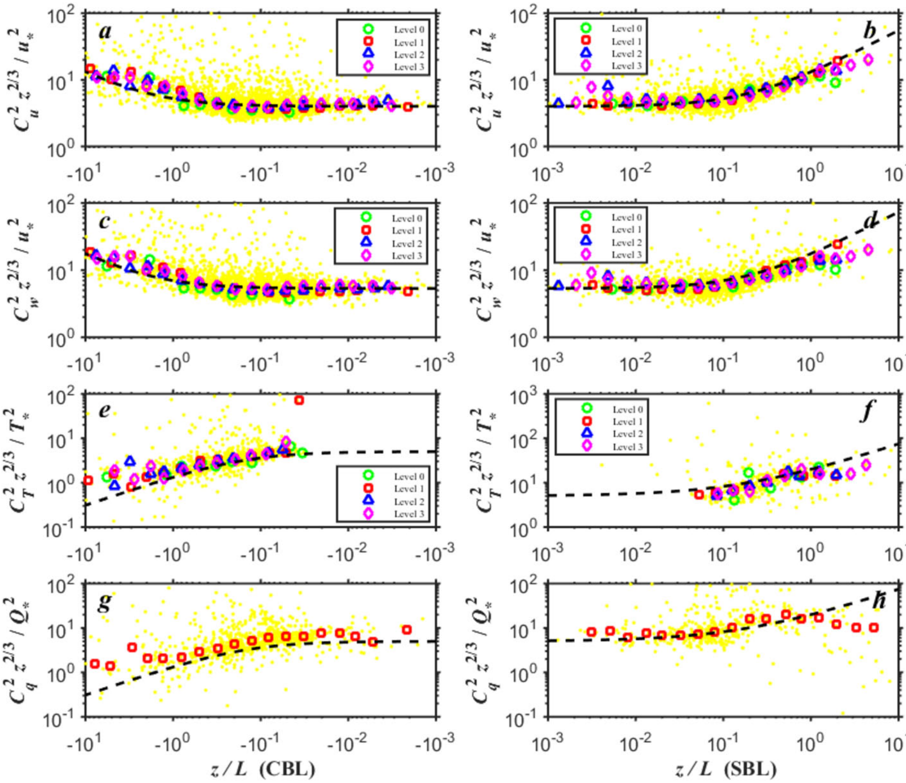

Fig. 10 The bin-averaged nondimensional structure parameters of the **a**, **b** longitudinal and **c**, **d** vertical velocity components, **e**, **f** air temperature, and **g**, **h** specific humidity plotted in log–log coordinates versus the local MOST stability parameter (9) for the 30-min averaged data collected over the water at the FRF Pier tower during the CASPER-East field campaign. Plots in the left panels (a, c, e, g) correspond to unstable conditions, or CBL, $\zeta < 0$; the right panels (b, d, f, h) represent stable conditions, or SBL, > 0. The black dashed lines correspond to the Kaimal and Finnigan (1994) relationships (14) and (15) with $\varphi_{cw2}(\zeta) = (4/3)$ and $\varphi_{cq2}(\zeta)$ $\varphi_{Cq2}(\zeta) = \varphi_{CT2}(\zeta)$. Individual 30-min averaged data-points for all measurement levels are shown as the background yellow dot-symbols

small and asymptotically tends to zero as ζ approaches zero, whereas, in the near-neutral case the value of C_T^2 is small but still finite. While the scatter is larger for the C_T^2 case, the data essentially follow the MOST canonical curves except for near-neutral and very highly stable/unstable cases. This behaviour of C_T^2 is very similar to the behaviour of σ_T reported by Grachev et al. (2018a. 2021). At the same time, our data for C_q^2 (Figs. 10, 11 and 12, panels g and h) systematically overestimate the empirical Kansas-type expressions by Kaimal and Finnigan (1994) for temperature, Eq. (15).

Note that MOST is a conceptual framework that is only applicable under ideal conditions, such as the assumptions of horizontal homogeneity, stationarity, and a constant flux layer. These assumptions are obviously violated in coastal zones. Because of the surface heterogeneity (patchiness) at different scales, the surface sources and sinks for heat and moisture are different that result in scalar dissimilarity between T and q in such conditions (e.g., Katul et al. 1995; Andreas et al. 1998; Detto et al. 2008 and references therein).

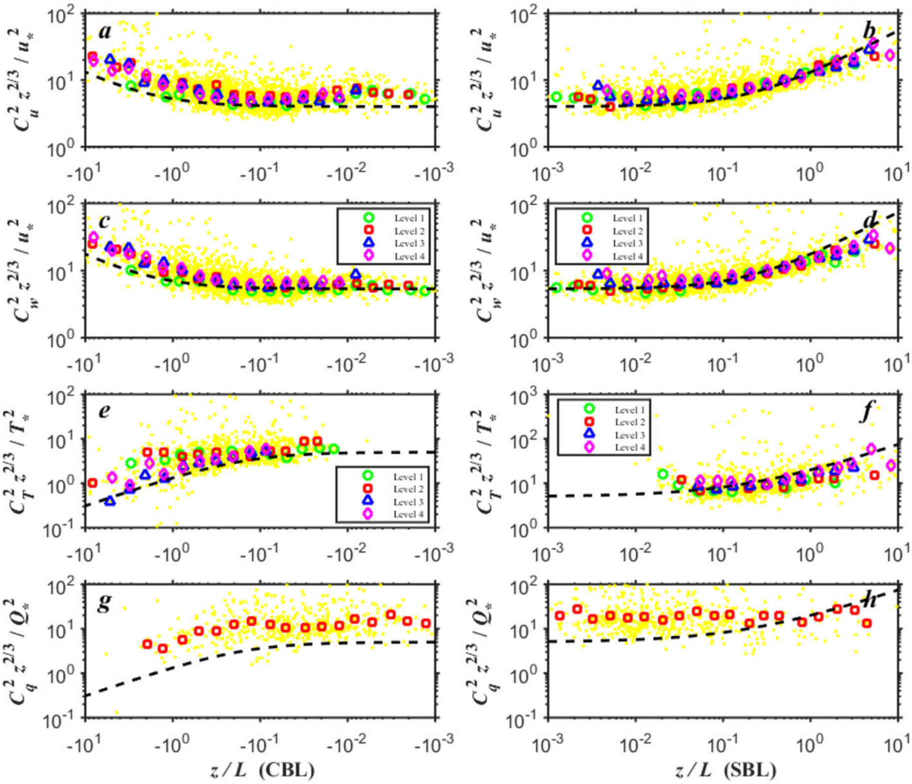

Fig. 11 Same as Fig. 10 but for the data collected over land at the FRF Video tower (panels *a*, *b*, *c*, *d*,*e*, and *f*) and the SDT tower (panels *g* and *h*) during the CASPER-East field campaign

4.4 Variance-Based Hybrid Scaling for the Structure Parameters

As noted in Sect. 2.2, some plots in the framework of the Monin–Obukhov approach (e.g., Figs. 10, 11 and 12) can be affected by self-correlation, and one method to overcome self-correlation is plotting a universal function in a "hybrid" representation without u_*; that is,

$$\frac{C_\alpha^2 z^{\frac{2}{3}}}{\sigma_\alpha^2} = f_{C\alpha 2}(\zeta), \tag{23}$$

where $\alpha = u, v, w, \theta$, or q and $= z/L$ is the Monin–Obukhov stability parameter for local scaling defined by (9). Figure 13 shows such plots of variance-based universal functions of the structure parameters normalized according to (23) versus ζ for the CASPER-East field campaign over the water at the FRF Pier tower. Similar plots for data over land at the FRF Video tower (panels a-f) and the SDT tower (panels g and h) are shown in Fig. 14. Figure 15 shows $f_{C\alpha 2}(\zeta)$ versus ζ for the data collected during C-FOG. Similar to Figs. 10, 11 and 12, the individual 30-min averaged (Figs. 13 and 14) and 15-min-averaged (Fig. 15) data-points of normalized C_α^2 for all measurement levels are also shown in Figs. 12, 13 and 14 as background yellow dot-symbols. Recall that Figs. 13, 14 and 15 by definition do not contain self-correlations because "new" universal functions $f_{C\alpha 2} = \varphi_{C\alpha 2}\varphi_\alpha^{-2}$ share no variables with

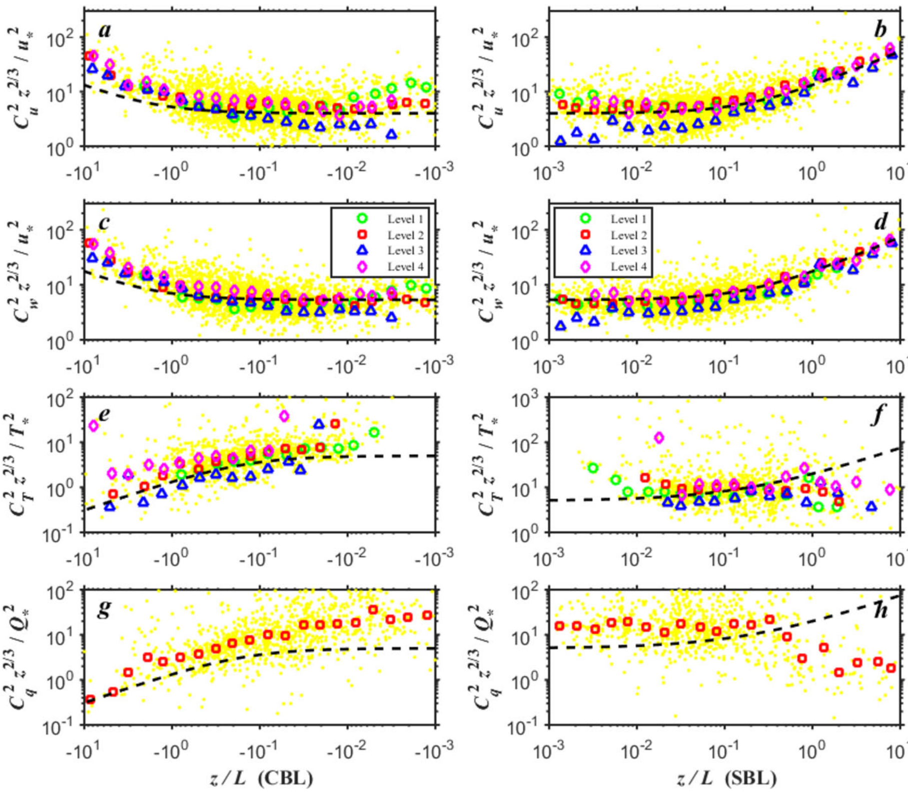

Fig. 12 Same as Fig. 10 but for the data collected at the UND tower located at The Downs measurement site in Ferryland, Newfoundland during the C-FOG field campaign. The data are based on 15-min averaging for clear sky days with high visibility (i.e., fog-free conditions) when the PWD22 visibility was greater than 6 km

ζ except a reference height z (e.g., see Eqs. 16–19). As such, plots in Figs. 13, 14 and 15 are more objective those in Figs. 10, 11 and 12.

Similar to the traditional MOST, the exact forms of the universal functions (23) cannot be predicted and must be determined from measurements, except for asymptotic cases of very stable ($\gg 1$) and very unstable (free convection, $\ll -1$) stratifications. In the very stable case, stratification inhibits vertical motions and the turbulence no longer communicates significantly with the surface. In this case, the dependence of z is expected to cease, leading to $f_{C\alpha 2}() \propto z^{2/3} \propto {}^{2/3}$. According to MOST, in the free convection limit ($\ll -1$) the friction velocity becomes insignificant, and u_* ceases to be a scaling parameter in (23). This assumption leads to the fact that the universal functions $f_{C\alpha 2}(\zeta)$ become asymptotically constant for $\ll -1$. In the neutral case ($= 0$) the functions (23) are constant by definition. Thus, under unstable conditions a function $f_{C\alpha 2}()$ is an interpolation which provides blending between two constants that may be close to each other; that is, $f_{C\alpha 2}(0) \approx f_{C\alpha 2}(\rightarrow -\infty)$.

According to Figs. 13, 14 and 15, the nondimensional universal functions (23) for variables $\alpha = u, w, T$, and q measured in the coastal zones, on the average, follow this conclusion for unstable (< 0) stratification. The behaviour of a function interpolating between two asymptotic constants for < 0, however, is different for different variables. Specifically, the

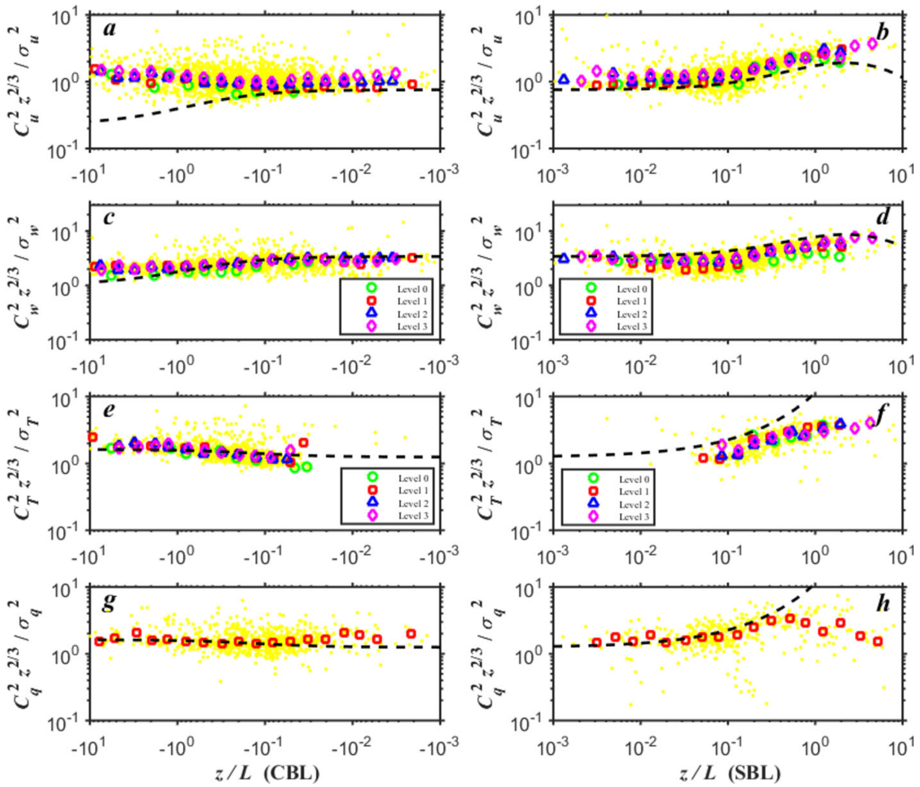

Fig. 13 The bin-averaged nondimensional structure parameters structure parameters of the **a**, **b** longitudinal and **c**, **d** vertical velocity components, **e**, **f** air temperature, and **g**, **h** specific humidity based on the variance hybrid scaling (23) plotted in log–log coordinates versus the local MOST stability parameter (9) for the 30-min averaged data collected over the water at the FRF Pier tower during the CASPER-East field campaign. Plots in the left panels (*a*, *c*, *e*, *g*) correspond to unstable conditions, or CBL, <0; the right panels (*b*, *d*, *f*, *h*) represent stable conditions, or SBL, >0. The black dashed lines are based on the Kaimal and Finnigan (1994) relationships for C_α^2 and σ_α^2 where $\alpha = u$, v, w, T, or q. Individual 30-min averaged data points for all measurement levels are shown as the background yellow dot-symbols

nondimensional structure parameter (23) for humidity ($\alpha = q$) weakly depends on stratification for convective conditions, if it depends on ζ at all (see Figs. 13, 14 and 15, panels g). In other words, the asymptotic constants in the free-convection limit and the near-neutral stratification are close to each other, i.e., $f_{Cq2}() \approx const$ for <0. The nondimensional universal functions (23) for the velocity components, change weakly for <0 (see Figs. 13, 14 and 15, panels a and c). The strongest variations of Eq. 23 are generally observed for the air temperature ($\alpha = T$), and the asymptotic value in the free-convection limit $f_{CT2}(\rightarrow -\infty)$ is generally larger than for the neutral case $f_{CT2}(0)$ (see Figs. 13, 14 and 15, panels e). For the case of stable stratification >0 (Figs. 13, 14 and 15, panels b, d, f, and h), the nondimensional universal functions (23) for all variables generally increase monotonically with increasing $= z/L$, consistent with the z-less prediction $f_{C\alpha 2}(\zeta) \propto \zeta^{2/3}$ (maybe with some exception for $\alpha = q$ case under very stable conditions).

Although traditional plots of the universal functions versus the stability parameter (9) in Figs. 10, 11, 12, 13, 14 and 15 are useful general tools, additional detailed information

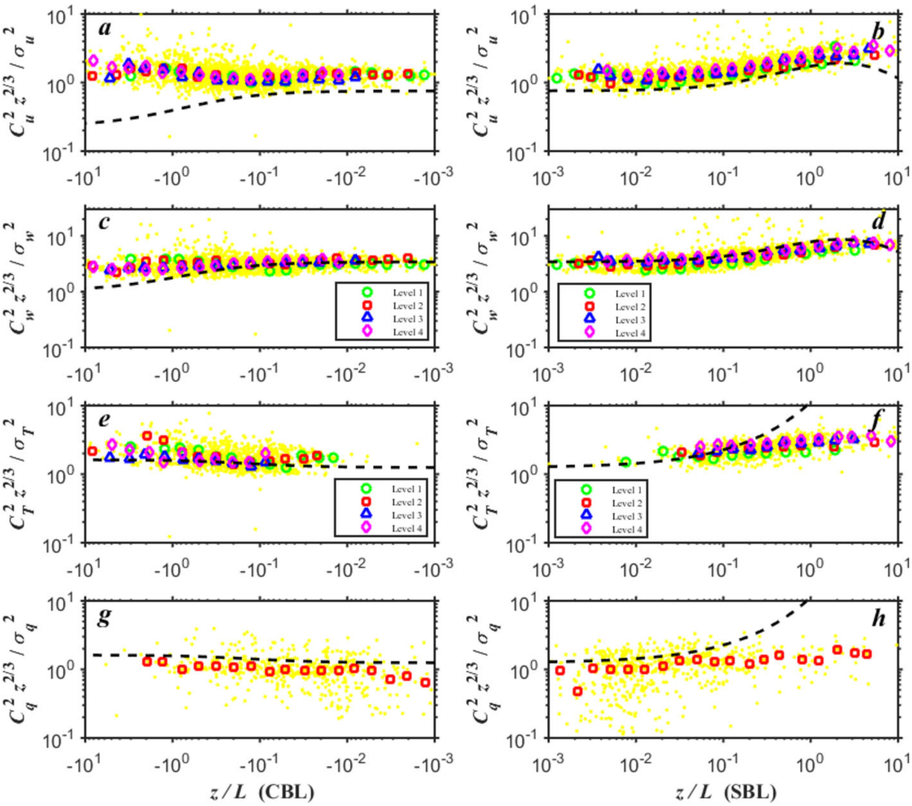

Fig. 14 Same as Fig. 13 but for the data collected over land at the FRF Video tower (panels *a*, *b*, *c*, *d*,*e*, and *f*) and the SDT tower (panels *g* and *h*) during the CASPER-East field campaign

can be obtained if the data collected in a coastal zone are divided into onshore and offshore cases. Figure 16 shows bin-averaged dependencies of the variance hybrid scaling $C_\alpha^2 z^{2/3}/\sigma_\alpha^2$ (Eq. 23) for variables $\alpha = u, w, T$, and q plotted against z/L separately for onshore and offshore winds measured over land at the FRF Video and SDT towers during the CASPER-East field campaign at (as the most illustrative example). Recall that the onshore wind directions range from 342° through 162° clockwise (dash-dot vertical lines in Fig. 9). According to Fig. 16, the bin-averaged data of $C_\alpha^2 z^{2/3}/\sigma_\alpha^2$ observed during onshore winds (colour solid lines) are generally not very different from those observed with offshore winds (colour dashed lines), although the dashed lines are often slightly lower than the solid lines. Moreover, the bin-averaged data observed at different levels for both onshore and offshore winds collapse fairly well into a single universal curve (especially for the scaled C_w^2).

Another advantage of the variance-based scaling (23) compared to the traditional MOST is the absence of the ambiguity for the dimensionless temperature structure parameter $f_{CT2}(\zeta)$ for near-neutral conditions $|| \to 0$ as compared with $\varphi_{CT2}(\zeta)$ (cf. Figures 10, 11 and 12 and Figs. 13, 14 and 15, panels e and f). This is due to the fact that the temperature scale T_* in (11) is small and asymptotically tends to zero as $\to 0$, whereas, in the near-neutral case σ_T is small but still finite (see also discussion in Grachev et al. 2018a). This behaviour of σ_T is associated with a surface that is thermally inhomogeneous wherein local hot and cold spots

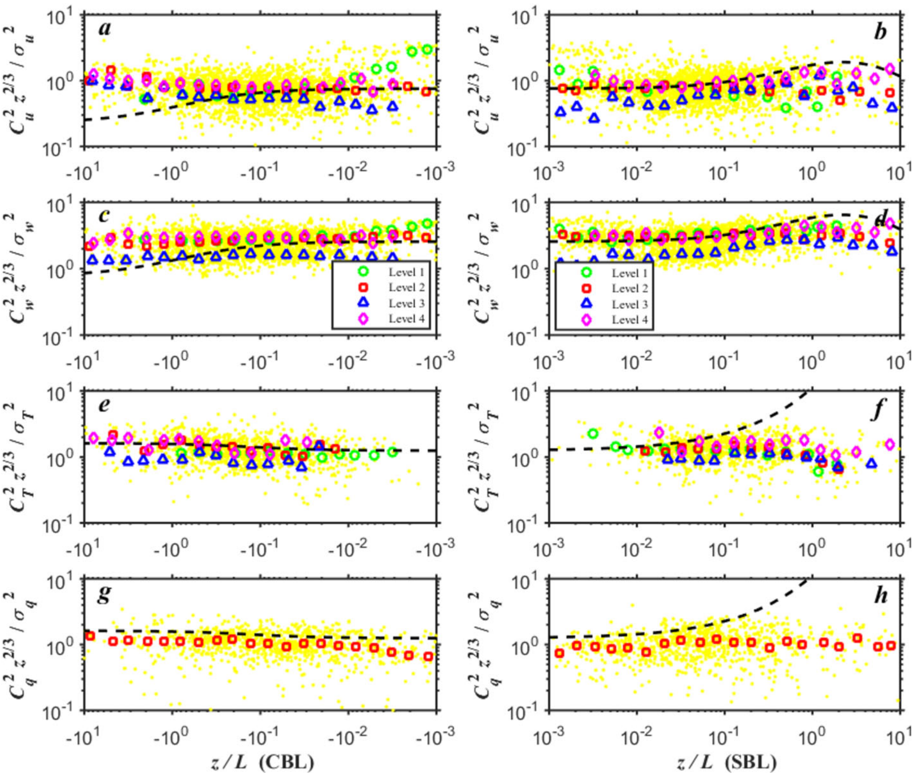

Fig. 15 Same as Fig. 13 but for the data collected at the UND tower located at The Downs measurement site in Ferryland, Newfoundland during the C-FOG field campaign. The data are based on 15-min averaging for clear sky days with high visibility (i.e., fog-free conditions) when the PWD22 visibility was greater than 6 km

on the surface generate small-scale advection that enhances σ_θ but not the surface fluxes, i.e., T_*. This argument is less applicable for σ_q and $\varphi_{Cq2}(\zeta)$, where $|Q_*|$ need not be small in near-neutral conditions.

Finally, we also note that the variance-based hybrid scaling (23) can be potentially implemented in a second-order turbulence closure like COAMPS (Coupled Ocean–Atmosphere Mesoscale Prediction System) for C_n^2 parameterization, since in the model a scalar structure parameter is related to relevant scalar variance (Wang et al. 2020 their Eq. 3). It should be also noted that the hybrid scaling method is an addition (not an alternative) to MOST that allows testing parameterizations and analyzing field data that are not affected by spurious self-correlation.

5 Summary and Discussion

The study reported herein concerned the structure–function parameters (or just structure parameters) of velocity, temperature, and specific humidity and other ancillary information in the atmospheric boundary layer at two coastal sites; one on the Outer Banks between the Atlantic Ocean and the Currituck Sound near the town of Duck, North Carolina (CASPER-East Program) and the other located near the town of Ferryland, Newfoundland, Canada

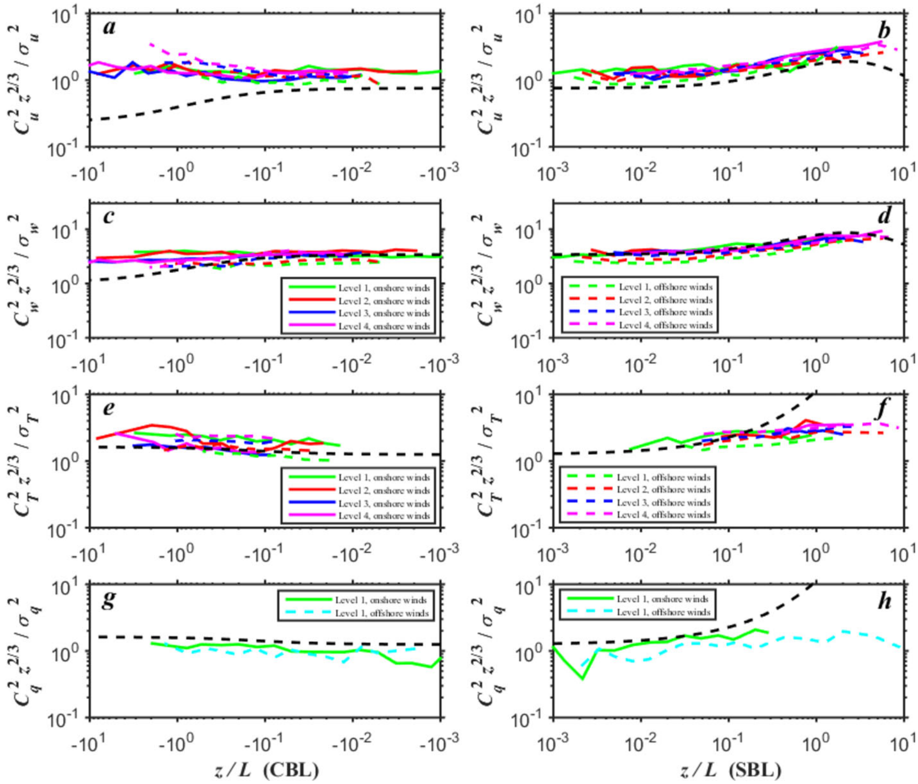

Fig. 16 The bin-averaged nondimensional structure parameters structure parameters of the **a**, **b** longitudinal and **c**, **d** vertical velocity components, **e**, **f** air temperature, and **g**, **h** specific humidity based on the variance hybrid scaling (23) plotted in log–log coordinates versus the local MOST stability parameter (9) for the 30-min averaged data collected over land at the FRF Video tower (panels *a*, *b*, *c*, *d*,*e*, and *f*) and the SDT tower (panels *g* and *h*) during the CASPER-East field campaign (same as Fig. 13 but separately for onshore and offshore winds). Plots in the left panels (*a*, *c*, *e*, *g*) correspond to unstable conditions, or CBL, <0; the right panels (*b*, *d*, *f*, *h*) represent stable conditions, or SBL, >0. The coloured solid and dashed lines correspond to onshore and offshore cases, respectively. The black dashed lines are based on the Kaimal and Finnigan (1994) relationships for C_α^2 and σ_α^2 where $\alpha = u, v, w, T$, or q

(C-FOG field campaign). Turbulence and mean meteorological data were collected at multiple levels (up to four) on several meteorological towers deployed on land at different distances from the shoreline, with one tower located at the end of a 560-m-long pier i.e., "over water". Overall, the data allowed the study of the structure parameters and other statistics for different surface footprints, including relatively smooth sea surface conditions and aerodynamically rough dry inland areas for both stable and unstable stratifications. Details regarding the observation sites, various measurements at these locations, turbulent data processing, accuracy of measurements, calibration, data-quality criteria etc. in detail can be found in Grachev et al. (2018a), Wang et al. (2018) for the CASPER-East and in Bardoel et al. (2021), Dorman et al. (2021), Fernando et al. (2021), Grachev et al. (2021), and Perelet et al. (2021) for the C-FOG programs.

A coastal zone is the interface between water and land footprints, signifying a transition between surfaces with completely different mechanical and thermal properties. For onshore flow, this leads to the formation of a thin internal boundary layer (IBL) often resolved by the towers used (see Figs. 1 and 2). The drag coefficient, diurnal variation of the sensible heat flux, and the Bowen ratio, among other parameters, were considered as coastal IBL markers. In particular, a coastal IBL in the case of onshore winds is associated with high values of the 10-m neutral drag coefficient ($C_{Dn10} \sim 10^{-2}$–10^{-1}), strong diurnal variations of H_S and T/RH, and $|\mathrm{Bo}| > 1$.

Understanding the behaviour of the structure parameters is important for wave propagation in the turbulent atmosphere. Time series of the dimensional structure parameters measured at different towers and different observation levels at the two coastal zones were analysed first. The lower values of the dimensional structure parameters were associated with higher altitudes, smooth surfaces (e.g., over water), and stable stratifications (e.g., for nocturnal boundary layer), ceteris paribus. The structure parameters over a land footprint could be an order of magnitude larger than that over the sea surface due to the change in aerodynamic and thermal properties of the surface. Another marked difference was the stronger diurnal cycle evident in the scalar (temperature and specific humidity) structure parameters, C_T^2 and C_q^2, observed over land due to the disparate heat capacities of water and soil. Specifically, a diurnal cycle was observed in C_T^2 during CASPER-East and C-FOG as well as C_q^2 in C-FOG.

The applicability of Monin–Obukhov similarity theory (MOST) to velocity and scalar structure parameters in the coastal zones over different footprint surfaces and for both stable and unstable conditions was studied. Specifically, the MOST nondimensional universal functions $\varphi_{C\alpha}(\zeta)$ for velocity components ($\alpha = u, w$) and scalars ($\alpha = T, q$) were plotted as a function of the stability parameter, $= z/L$ at each observational level (local scaling) and compared with the relationships (14) and (15) of Kaimal and Finnigan (1994). As we have shown previously (Grachev et al. 2018a; 2021), under conditions that violate the horizontal homogeneity assumptions underlying MOST (e.g., in coastal zones), different universal functions behave differently. While the non-dimensional profiles of wind speed and temperature fail to predict fluxes correctly, e.g., vertical turbulent fluxes may contradict local gradients (Grachev et al. 2018a, at Figs. 14 and 15), the properly scaled standard deviations and the dissipation rate generally obey MOST. According to current study, the nondimensional structure parameters of the velocity components measured at the Outer Banks (North Carolina) and Ferryland (Newfoundland), in general, also follow MOST local scaling for both stable (> 0) and unstable (< 0) stratifications (Figs. 10, 11 and 12). Furthermore, the data for different measurement levels collected over water footprints collapse into a single universal curve with surprisingly small scatter (especially for the scaled statistics of the velocity components). Observations, however, showed a slightly poor correspondence (e.g., a bias and relatively larger scatter) to the MOST nondimensional structure parameters for scalars, air temperature, $\varphi_{CT2}(\zeta)$, and specific humidity, $\varphi_{Cq2}(\zeta)$ when compared with Kaimal-Finnigan parameterizations (see Figs. 10, 11 and 12, panels e, f, g, and h).

It can be assumed that that such different behaviour of various MOST universal functions versus $= z/L$ is associated with a combination of local and non-local turbulent transport in the ABL. While the single-point statistics of turbulence such as the scaled standard deviations and the structure parameters depend heavily on the small-scale turbulent mixing, the non-dimensional profiles of wind speed and temperature are based on coarse-resolution measurements in a layer of several metres thickness and, thus, are controlled by both small-scale eddy diffusion as well as large-scale circulations. The larger-size eddies can transport momentum and heat through the entire depth of the ABL (non-local mixing), or they may also be constrained by IBL height and the coastal terrain geometry. It is evident that the non-local transport in the ABL is overlooked by traditional MOST, e.g., large-scale coherent structures embracing the entire convective boundary layer (Golitsyn and Grachev 1986; Godfrey and Beljaars 1991; Sykes et al. 1993; Grachev et al. 1997; Fairall et al. 2003; Zilitinkevich et al. 2006). Recall that MOST is based on the mixing length theory for the small-scale turbulence, and it is reasonable to expect that the single-point statistics of turbulence generally obey MOST even over inhomogeneous surfaces, such as coastal zones (see further discussion in Grachev et al. 2018a). It should be noted that non-local effects in general also influence measurements at one point (mainly on σ_u and σ_v), but this influence is not as critical as in the case of vertical gradients measured in a layer several meters thick.

A new variance-based scaling was suggested for the structure parameters, which remedies some of the shortcomings of the traditional MOST approach, such as self-correlation and ambiguity of $\varphi_{CT2}(\zeta)$ for near-neutral conditions. This is based on the idea that a combination of any traditional Monin–Obukhov universal functions is itself a universal function. Proposed "hybrid" representation is not affected by the self-correlation because the new universal function shares no variables with the MOST stability parameter $= z/L$. Specifically, a "new" universal function is defined as the ratio $f_{C\alpha 2}(\zeta) = (\zeta)/(\zeta)$, where (ζ) is the nondimensional standard deviation ($\alpha = u, v, w, T$, or q). Formally, if u_*^2, T_*^2 or Q_*^2 in ζ are replaced by a suitable σ_α^2, then $f_{C\alpha 2}$ is recovered. Plots of $f_{C\alpha 2} = C_\alpha^2 z^{2/3}/\sigma_\alpha^2$ versus $= z/L$ are shown in Fig. 13, 14 and 15. In particular, the new universal function $f_{C\alpha 2}(\zeta)$ for < 0 is an interpolation that provides blending between two constants that may be close to each other $f_{C\alpha 2}(0) \approx f_{C\alpha 2}(\rightarrow -\infty)$; that is, $f_{C\alpha 2}()$ is weakly dependent on stratification for convective conditions, if it depends on ζ at all. In addition, the nondimensional structure parameter for the air temperature $f_{CT2}(\zeta)$ contains no flaws associated with the ambiguity for near-neutral conditions $||\rightarrow 0$ as compared with the traditional MOST universal function $\varphi_{CT2}(\zeta)$.

Acknowledgements Any opinions expressed in this paper are those of the authors and do not necessarily reflect the official policy or position of the U.S. Department of the Army, the Department of Defence, the U.S. Government, or the funding agency. This work was also performed within the framework of the CASPER Program funded by the Office of Naval Research (ONR) under its Multidisciplinary University Research Initiative (MURI) program, grant N00014-17-1-3195 to University of Notre Dame. The C-FOG research of University of Notre Dame was funded by ONR under the Award # N00014-18-1-2472 entitled: "Toward Improving Coastal Fog Prediction (C-FOG)". The work of this paper was also partially funded by the Grant N00014-21-1-2296 (Fatima Multidisciplinary University Research Initiative) of the Office of Naval Research, administered by the Marine Meteorology and Space Program for University of Notre Dame. We thank all who organized, deployed, operated, and maintained instrumentation that provided a valuable set of in situ measurements during the CASPER-East and C-FOG field campaigns. Their diligent and dedicated efforts are greatly appreciated. The authors also gratefully acknowledge the three anonymous reviewers for their thoughtful and detailed feedback. Their critical comments and constructive suggestions have substantially improved the manuscript. Special thanks go to Drs. Igor Petenko, Valery Zavorotny, Vladimir Ostashev, and Evgeni Fedorovich for numerous discussions of wave propagation in a turbulent atmosphere.

Author Contributions All authors contributed to discussing the results and to reviewing and editing the manuscript. A.A.G. developed the methodology, wrote the main manuscript text, prepared all figures, and developed the associated software. A.A.G., S.L.B., and L.S.L. processed the turbulence and surface meteorological datasets. H.J.S.F., R.M.R., and C.M.H. contributed to the implementation and supervision of the field programs. A.A.G., H.J.S.F., S.L.B., E.D.C., and L.S.L. participated in the field expeditions.

Funding DEVCOM Army Research Laboratory, Office of Naval Research, N00014-17-1-3195, N00014-18-1-2472, N00014-17-1-3195

Data Availability No datasets were generated or analysed during the current study.

Declarations

Conflict of interest The authors declare no competing interests.

References

Alappattu DP, Wang Q, Yamaguchi RT, Haack T, Ulate M, Fernando HJ, Frederickson P (2022) Electromagnetic ducting in the near-shore marine environment: results from the CASPER-East field experiment. J Geophys Res 127(22):e2022JD037423. https://doi.org/10.1029/2022JD037423

Andreas EL (1988) Estimating Cn2 over snow and sea ice from meteorological data. J Opt Soc Am A Opt Image Sci 5(4):481–495. https://doi.org/10.1364/JOSAA.5.000481

Andreas EL (1989) The refractive index structure parameter, C<sub />2n, for a year over the frozen Beaufort Sea. Radio Sci 24(5):67–679. https://doi.org/10.1029/RS024i005p00667

Andreas EL, Hicks BB (2002) Comments on "critical test of the validity of Monin-Obukhov similarity during convective conditions." J Atmos Sci 59(17):2605–2607

Andreas EL, Hill RJ, Gosz JR, Moore DI, Otto WD, Sarma AD (1998) Statistics of surface-layer turbulence over terrain with metre-scale heterogeneity. Boundary-Layer Meteorol 86(3):379–408. https://doi.org/10.1023/A:1000609131683

Andreas EL, Horst TW, Grachev AA, Persson POG, Fairall CW, Guest PS, Jordan RE (2010a) Parametrizing turbulent exchange over summer sea ice and the marginal ice zone. Q J R Meteorol Soc 136(649B):927–943. https://doi.org/10.1002/qj.618

Andreas EL, Persson POG, Jordan RE, Horst TW, Guest PS, Grachev AA, Fairall CW (2010b) Parameterizing turbulent exchange over sea ice in winter. J Hydrometeorol 11(1):87–104. https://doi.org/10.1175/2009JHM1102.1

Andreas EL, Mahrt L, Vickers D (2012) A new drag relation for aerodynamically rough flow over the ocean. J Atmos Sci 69(8):2520–2537. https://doi.org/10.1175/JAS-D-11-0312.1

Aristidi E, Vernin J, Fossat E, Schmider F-X, Travouillon T, Pouzenc C, Traullé O, Genthon C, Agabi A, Bondoux E, Challita Z, Mékarnia D, Jeanneaux F, Bouchez G (2015) Monitoring the optical turbulence in the surface layer at Dome C, Antarctica, with sonic anemometers. Mon Not R Astron Soc 454(4):4304–4315. https://doi.org/10.1093/mnras/stv2273

Baas P, Steeneveld GJ, van de Wiel BJH, Holtslag AAM (2006) Exploring self-correlation in flux-gradient relationships for stably stratified conditions. J Atmos Sci 63(11):3045–3054

Bardoel SL, Horna Muñoz DV, Grachev AA, Krishnamurthy R, Chamorro LP, Fernando HJS (2021) Fog formation related to gravity currents interacting with coastal topography. Boundary-Layer Meteorol 181(2–3):499–521. https://doi.org/10.1007/s10546-021-00638-w

Bardoel SL, Hoch S, Ruiz-Plancarte J, Lenain L, Gultepe I, Grachev AA, Gaberšek A, Wang Q, Fernando HJS (2025) Study of fog dissipation in an internal boundary layer on Sable Island. Q J R Meteorol Soc 151(766A):e4891. https://doi.org/10.1002/qj.4891

Basu S (2015) A simple approach for estimating the refractive index structure parameter (Cn2) profile in the atmosphere. Opt Lett 40(17):4130–4133. https://doi.org/10.1364/OL.40.004130

Basu S, Holtslag AAM (2022) Revisiting and revising Tatarskii's formulation for the temperature structure parameter (CT2) in atmospheric flows. Environ Fluid Mech 22(5):1107–1119. https://doi.org/10.1007/s10652-022-09880-3

Beyrich F, Kouznetsov RD, Leps J-P, Lüdi A, Meijninger WML, Weisensee U (2005) Structure parameters for temperature and humidity from simultaneous eddy-covariance and scintillometer measurements. Meteorol Z 14(5):641–649. https://doi.org/10.1127/0941-2948/2005/0064

Braam M, Moene AF, Beyrich F, Holtslag AAM (2014) Similarity relations for CT2 in the unstable atmospheric surface layer: dependence on regression approach, observation height and stability range. Boundary-Layer Meteorol 153(1):63–87. https://doi.org/10.1007/s10546-014-9938-y

Burba G (2013) Eddy covariance method for scientific, industrial, agricultural and regulatory applications: a field book on measuring ecosystem gas exchange and areal emission rates. LI-COR Biosciences, Lincoln, USA, 331 pp. ISBN: 978–0–61576827–4

Cherubini T, Businger S (2013) Another look at the refractive index structure function. J Appl Meteor Climatol 52(2):498–506. https://doi.org/10.1175/JAMC-D-11-0263.1

Coceal O, Belcher SE (2004) A canopy model of mean winds through urban areas. Q J R Meteorol Soc 130(599):1349–1372. https://doi.org/10.1256/qj.03.40

Cuxart J, Boone AA (2020) Evapotranspiration over land from a boundary-layer meteorology perspective. Boundary-Layer Meteorol 177(2–3):427–459. https://doi.org/10.1007/s10546-020-00550-9

Detto M, Katul G, Mancini M, Montaldo N, Albertson JD (2008) Surface heterogeneity and its signature in higher-order scalar similarity relationships. Agric Forest Meteorol 148(6–7):902–916. https://doi.org/10.1016/j.agrformet.2007.12.008

Dorman CE, Grachev AA, Gultepe I, Fernando HJS (2021) Toward improving coastal-fog prediction (C-FOG). Boundary-Layer Meteorol 181(2–3):167–170. https://doi.org/10.1007/s10546-021-00664-8

Dorman CE, Mejia J, Koračin D, McEvoy D (2017) Worldwide marine fog occurrence and climatology. In: Koračin D, Dorman CE (Eds.) Marine fog: Challenges and advancements in observations, modeling, and forecasting, Chapter 2. 7–152. Springer International Publishing Switzerland. https://doi.org/10.1007/978-3-319-45229-6_2

Fahey T, Islam M, Gardi A, Sabatini R (2021) Laser beam atmospheric propagation modelling for aerospace LIDAR applications. Atmos 12(7):918. https://doi.org/10.3390/atmos12070918

Fairall CW (1991) The humidity and temperature sensitivity of clear-air radars in the convective boundary layer. J Appl Meteor Climatol 30(8):1064–1074

Fairall CW, Bradley EF, Hare JE, Grachev AA, Edson JB (2003) Bulk parameterization of air-sea fluxes: updates and verification for the COARE algorithm. J Clim 16(4):571–591

Fairall CW, Bariteau L, Grachev AA, Hill RJ, Wolfe DE, Brewer WA, Tucker SC, Hare JE, Angevine WM (2006) Turbulent bulk transfer coefficients and ozone deposition velocity in the international consortium for atmospheric research into transport and transformation. J Geophys Res 111(D23):D23S20. https://doi.org/10.1029/2006JD007597

Fernando HJS, Gultepe I, Dorman C, Pardyjak E, Wang Q, Hoch SW, Richter D, Creegan E, Gaberšek S, Bullock T, Hocut C, Chang R, Alappattu D, Dimitrova R, Flagg D, Grachev A, Krishnamurthy R, Singh DK, Lozovatsky I, Nagare B, Sharma A, Wagh S, Wainwright C, Wroblewski M, Yamaguchi R, Bardoel S, Coppersmith RS, Chisholm N, Gonzalez E, Gunawardena N, Hyde O, Morrison T, Olson A, Perelet A, Perrie W, Wang S, Wauer B (2021) C-FOG: life of coastal fog. Bull Am Meteorol Soc 102(2):E244–E272. https://doi.org/10.1175/BAMS-D-19-0070.1

Fiorino S, Bose-Pillai S, Keefer K (2021) Re-visiting acoustic sounding to advance the measurement of optical turbulence. Appl Sci 11(16):7658. https://doi.org/10.3390/app11167658

Foken T (2017) Micrometeorology. Second Edition, Springer-Verlag, Berlin Heidelberg, 362 p. https://doi.org/10.1007/978-3-642-25440-6

Frederickson PA, Davidson KL, Zeisse CR, Bendall CS (2000) Estimating the refractive index structure parameter (Cn2) over the ocean using bulk methods. J Appl Meteorol Climatol 39(10):1770–1783. https://doi.org/10.1175/1520-0450-39.10.1770

Frehlich R, Sharman R, Vandenberghe F, Yu W, Liu Y, Knievel J, Jumper G (2010) Estimates of Cn2 from numerical weather prediction model output and comparison with thermosonde data. J Appl Meteorol Climatol 49(8):1742–1755. https://doi.org/10.1175/2010JAMC2350.1

Fussman CR (2014) High energy laser propagation in various atmospheric conditions utilizing a new, accelerated scaling code. MSci Thesis. Naval Postgraduate School, Monterey, CA, USA, 91p. https://apps.dtic.mil/sti/pdfs/ADA607774.pdf

Garratt JR (1987) The stably stratified internal boundary-layer for steady and diurnally varying offshore flow. Bound-Layer Meteorol 38(4):369–394. https://doi.org/10.1007/BF00120853

Garratt JR (1990) The internal boundary-layer—a review. Bound-Layer Meteorol 50(1):171–203. https://doi.org/10.1007/BF00120524

Garratt JR (1992) The Atmospheric Boundary Layer. Cambridge University Press, U.K., p 316

Garratt JR, Ryan BF (1989) The structure of the stably stratified internal boundary-layer in offshore flow over the sea. Bound-Layer Meteorol 47(1):17–40. https://doi.org/10.1007/BF00122320

Geernaert GL (2002) On extending the flux-profile similarity theory to include quasi-homogeneous conditions in the marine atmospheric surface layer. Bound-Layer Meteorol 105(3):433–450. https://doi.org/10.1023/A:1020307703242

Gibbs JA, Fedorovich E (2020a) On the evaluation of the proportionality coefficient between the turbulence temperature spectrum and structure parameter. J Atmos Sci 77(8):2761–2763. https://doi.org/10.1175/jas-d-19-0344.1

Gibbs JA, Fedorovich E (2020b) Structure functions and structure parameters of velocity fluctuations in numerically simulated atmospheric convective boundary layer flows. J Atmos Sci 77(10):3619–3630. https://doi.org/10.1175/JAS-D-20-0038.1

Gibbs JA, Fedorovich E, Maronga B, Wainwright C, Dröse M (2016) Comparison of direct and spectral methods for evaluation of the temperature structure parameter in numerically simulated convective boundary layer flows. Mon Weather Rev 144(6):2205–2214. https://doi.org/10.1175/MWR-D-15-0390.1

Godfrey JS, Beljaars ACM (1991) On the turbulent fluxes of buoyancy, heat and moisture at the air-sea interface at low wind speeds. J Geophys Res 96(C12):22043–22048. https://doi.org/10.1029/91JC02015

Golitsyn GS, Grachev AA (1986) Free convection of multicomponent media and parameterization of air-sea interaction at light winds. Ocean-Air Interact 1:57–78

Grachev AA, Fairall CW, Zilitinkevich SS (1997) Surface-layer scaling for the convection-induced stress regime. Bound-Layer Meteorol 83(3):423–439. https://doi.org/10.1023/A:1000281625985

Grachev AA, Bariteau L, Fairall CW, Hare JE, Helmig D, Hueber J, Lang EK (2011) Turbulent fluxes and transfer of trace gases from ship-based measurements during TexAQS 2006. J Geophys Res 116:D13110. https://doi.org/10.1029/2010JD015502

Grachev AA, Andreas EL, Fairall CW, Guest PS, Persson POG (2012) Outlier problem in evaluating similarity functions in the stable atmospheric boundary layer. Bound-Layer Meteorol 144(2):137–155. https://doi.org/10.1007/s10546-012-9714-9

Grachev AA, Andreas EL, Fairall CW, Guest PS, Persson POG (2015) Similarity theory based on the Dougherty-Ozmidov length scale. Q J R Meteorol Soc 141(690A):1845–1856. https://doi.org/10.1002/qj.2488

Grachev AA, Leo LS, Fernando HJS, Fairall CW, Creegan E, Blomquist BW, Christman AJ, Hocut CM (2018a) Air-sea/land interaction in the coastal zone. Bound-Layer Meteorol 167(2):181–210. https://doi.org/10.1007/s10546-017-0326-2

Grachev AA, Persson POG, Uttal T, Akish EA, Cox CJ, Morris SM, Fairall CW, Stone RS, Lesins G, Makshtas AP, Repina IA (2018b) Seasonal and latitudinal variations of surface fluxes at two Arctic terrestrial sites. Clim Dyn 51(5–6):1793–1818. https://doi.org/10.1007/s00382-017-3983-4

Grachev AA, Krishnamurthy R, Fernando HJS, Fairall CW, Bardoel SL, Wang S (2021) Atmospheric turbulence measurements at a coastal zone with and without fog. Boundary-Layer Meteorol 181(2–3):395–422. https://doi.org/10.1007/s10546-021-00655-9

Grachev AA, Fairall CW, Blomquist BW, Fernando HJS, Leo LS, Otárola-Bustos SF, Wilczak JM, McCaffrey KL (2022) A hybrid bulk algorithm to predict turbulent fluxes over dry and wet bare soils. J Appl Meteorol Climatol 61(4):393–414. https://doi.org/10.1175/JAMC-D-20-0232.1

Grachev AA, Fairall CW, Blomquist BW, Fernando HJS, Leo LS, Otárola-Bustos SF, Wilczak JM, McCaffrey KL (2020) On the surface energy balance closure at different temporal scales. Agric Forest Meteorol 281. https://doi.org/10.1016/j.agrformet.2019.107823

Gur'yanov AE, Kallistratova MA, Martvel FE, Pekour MS, Petenko IV, Time NS, Shurygin EA (1987) Comparison of sodar and microfluctuation measurements of the temperature structure parameter in mountainous terrain. Izvestiya Atmos Ocean Phys 23(9):685–691

Hartogensis OK, De Bruin HAR (2005) Monin–Obukhov similarity functions of the structure parameter of temperature and turbulent kinetic energy dissipation rate in the stable boundary layer. Boundary-Layer Meteorol 116(2):253–276. https://doi.org/10.1007/s10546-004-2817-1

Hicks BB (1978) Comments on the characteristics of turbulent velocity components in the surface layer under convective conditions by H.A. Panofsky, H. Tennekes, D.H. Lenschow, and J.C. Wyngaard. Boundary-Layer Meteorol 15(2):255–258. https://doi.org/10.1007/BF00121926

Hill RJ (1989) Implications of Monin-Obukhov similarity theory for scalar quantities. J Atmos Sci 46(14):2236–2244

Hill RJ, Clifford SF, Lawrence RS (1980) Refractive-index and absorption fluctuations in the infrared caused by temperature, humidity, and pressure fluctuations. J Opt Soc Am 70(10):1192–1205. https://doi.org/10.1364/JOSA.70.001192

Hoedjes JCB, Chehbouni A, Ezzahar J, Escadafal R, De Bruin HAR (2007) Comparison of large aperture scintillometer and eddy covariance measurements: can thermal infrared data be used to capture footprint-induced differences? J Hydrometeorol 8(2):144–159. https://doi.org/10.1175/JHM561.1

Högström U, Hunt JCR, Smedman AS (2002) Theory and measurements for turbulence spectra and variances in the atmospheric neutral surface layer. Boundary-Layer Meteorol 103(1):101–124. https://doi.org/10.1023/A:1014579828712

Horst TW, Weil JC (1992) Footprint estimation for scalar flux measurements in the atmospheric surface layer. Boundary-Layer Meteorol 59(3):279–296. https://doi.org/10.1007/BF00119817

Horst TW, Weil JC (1994) How far is far enough?: the fetch requirements for micrometeorological measurement of surface fluxes. J Atmos Ocean Technol 11(4):1018–1025. https://doi.org/10.1175/1520-0426(1994)011%3c1018:HFIFET%3e2.0.CO;2

Kaimal JC (1973) Turbulence spectra, length scales and structure parameters in the stable surface layer. Bound-Layer Meteorol 4:289–309. https://doi.org/10.1007/BF02265239

Kaimal JC, Finnigan JJ (1994) Atmospheric Boundary Layer Flows: Their Structure and Measurements. Oxford University Press, New York and Oxford, p 289

Katul G, Goltz SM, Hsieh C, Cheng Y, Mowry F, Sigmon J (1995) Estimation of surface heat and momentum fluxes using the flux-variance method above uniform and non-uniform terrain. Bound-Layer Meteorol 74(3):237–260. https://doi.org/10.1007/BF00712120

Klipp C (2007) Wind direction dependence of atmospheric boundary layer turbulence parameters in the urban roughness sublayer. J Appl Meteorol Climatol 46(12):2086–2097. https://doi.org/10.1175/2006JAMC1298.1

Klipp CL, Mahrt L (2004) Flux-gradient relationship, self-correlation and intermittency in the stable boundary layer. Q J R Meteorol Soc 130(601B):2087–2103. https://doi.org/10.1256/qj.03.161

Kljun N, Calanca P, Rotach MW, Schmid HP (2004) A simple parameterisation for flux footprint predictions. Bound-Layer Meteorol 112(3):503–523. https://doi.org/10.1023/B:BOUN.0000030653.71031.96

Kljun N, Calanca P, Rotach MW, Schmid HP (2015) A simple two-dimensional parameterisation for flux footprint prediction (FFP). Geosci Model Dev 8:3695–3713. https://doi.org/10.5194/gmd-8-3695-2015

Kohsiek W (1982) Measuring CT2, CQ2, and CTQ in the unstable surface layer, and relations to the vertical fluxes of heat and moisture. Bound-Layer Meteorol 24(1):89–107. https://doi.org/10.1007/BF00121802

Kolmogorov AN (1941) The local structure of turbulence in incompressible viscous fluid for very large Reynolds numbers. Dokl Akad Nauk SSSR 30:301–305

Kooijmans LMJ, Hartogensis OK (2016) Surface-layer similarity functions for dissipation rate and structure parameters of temperature and humidity based on eleven field experiments. Boundary-Layer Meteorol 160(3):501–527. https://doi.org/10.1007/s10546-016-0152-y

Kormann R, Meixner FX (2001) An analytical footprint model for non-neutral stratification. Boundary-Layer Meteorol 99(2):207–224. https://doi.org/10.1023/A:1018991015119

Krishnamurthy R, Fernando HJS, Alappattu D, Creegan E, Wang Q (2023) Observations of offshore internal boundary layers. J Geophys Res 128(8):e2022JD037425. https://doi.org/10.1029/2022JD037425

Lange B, Johnson HK, Larsen S, Højstrup J, Kofoed-Hansen H, Yelland MJ (2004) On detection of a wave age dependency for the sea surface roughness. J Phys Oceanogr 34(6):1441–1458

Leclerc MY, Foken T (2014) Footprints in micrometeorology and ecology. Springer-Verlag Berlin Heidelberg, 239 pp. https://doi.org/10.1007/978-3-642-54545-0

Li D, Bou-Zeid E, De Bruin HAR (2012) Monin–Obukhov similarity functions for the structure parameters of temperature and humidity. Boundary-Layer Meteorol 145(1):45–67. https://doi.org/10.1007/s10546-011-9660-y

Lüdi A, Beyrich F, Mätzler C (2005) Determination of the turbulent temperature–humidity correlation from scintillometric measurements. Boundary-Layer Meteorol 117(3):525–550. https://doi.org/10.1007/s10546-005-1751-1

Mahrt L, Vickers D, Edson J, Sun J, Højstrup J, Hare J, Wilczak JM (1998a) Heat flux in the coastal zone. Boundary-Layer Meteorol 86(3):421–446. https://doi.org/10.1023/A:1000784219817

Mahrt L, Sun J, Blumen W, Delany T, Oncley S (1998b) Nocturnal boundary-layer regimes. Boundary-Layer Meteorol 88(2):255–278. https://doi.org/10.1023/A:1001171313493

Mahrt L, Andreas EL, Edson JB, Vickers D, Sun J, Patton EG (2016) Coastal zone surface stress with stable stratification. J Phys Oceanogr 46(1):95–105. https://doi.org/10.1175/JPO-D-15-0116.1

Mahrt L, Thomas CK, Grachev A, Persson POG (2018) Near-surface vertical flux divergence in the stable boundary layer. Boundary-Layer Meteorol 169(3):373–393. https://doi.org/10.1007/s10546-018-0379-x

Mahrt L, Nilsson E, Rutgersson A, Pettersson H (2021) Vertical divergence of the atmospheric momentum flux near the sea surface at a coastal site. J Phys Oceanogr 51(11):3529–3537. https://doi.org/10.1175/JPO-D-21-0081.1

Maronga B, Moene AF, van Dinther D, Raasch S, Bosveld GB (2013) Derivation of structure parameters of temperature and humidity in the convective boundary layer from large-eddy simulations and implications for the interpretation of scintillometer observations. Boundary-Layer Meteorol 148(1):1–30. https://doi.org/10.1007/s10546-013-9801-6

Maronga B, Hartogensis OK, Raasch S, Beyrich F (2014) The effect of surface heterogeneity on the structure parameters of temperature and specific humidity: a large-eddy simulation case study for the LITFASS-2003 experiment. Boundary-Layer Meteorol 153(3):441–470. https://doi.org/10.1007/s10546-014-9955-x

Meijninger WML, Beyrich F, Lüdi A, Kohsiek W, De Bruin HAR (2006) Scintillometer-based turbulent fluxes of sensible and latent heat over a heterogeneous land surface—a contribution to LITFASS-2003. Boundary-Layer Meteorol 121(1):89–110. https://doi.org/10.1007/s10546-005-9022-8

Moene AF (2003) Effects of water vapour on the structure parameter of the refractive index for near-infrared radiation. Boundary-Layer Meteorol 107(3):635–653. https://doi.org/10.1023/A:1022807617073

Moene AF, Meijninger, WML, Hartogensis OK, Kohsiek W, De Bruin HAR (2004) A review of the relationships describing the signal of a large aperture Scintillometer. Internal Report 2004/2. Meteorology and Air Quality Group, Wageningen University, Wageningen, the Netherlands, 40 pp

Monin AS, Obukhov AM (1954) Basic laws of turbulent mixing in the surface layer of the atmosphere. Tr Geofiz Inst Akad Nauk SSSR 24(151):163–187

Obukhov AM (1946) Turbulence in an atmosphere with a non-uniform temperature. Tr Inst Teoret Geofiz Akad Nauk SSSR 1:95–115 ((**translation in: Boundary-Layer Meteorol 1971 2:7–29**))

Ortiz-Suslow DG, Wang Q (2019) An evaluation of Kolmogorov's −5/3 power law observed within the turbulent airflow above the ocean. Geophys Res Lett 46(24):14901–14911. https://doi.org/10.1029/2019GL085083

Ortiz-Suslow DG, Haus BK, Williams NJ, Graber HC, MacMahan JH (2018) Observations of air-sea momentum flux variability across the inner shelf. J Geophys Res 123(12):8970–8993. https://doi.org/10.1029/2018JC014348

Ortiz-Suslow DG, Kalogiros J, Yamaguchi R, Wang Q (2021) An evaluation of the constant flux layer in the atmospheric flow above the wavy air-sea interface. J Geophys Res 126(8):e2020JD032834. https://doi.org/10.1029/2020JD032834

Ostashev VE, Wilson DK (2015) Acoustics in Moving Inhomogeneous Media, 2nd edn. CRC Press, Boca Raton FL, p 521

Peltier LJ, Wyngaard JC (1995) Structure-function parameters in the convective boundary layer from large-eddy simulations. J Atmos Sci 52(21):3641–3660

Perelet AO, Gultepe I, Hoch SW, Pardyjak ER (2021) Discriminating fog and rain at the kilometre scale using the extinction from collocated infrared and microwave scintillometers. Boundary-Layer Meteorol 181(2–3):295–315. https://doi.org/10.1007/s10546-021-00609-1

Perelet AO, Ward HC, Stoll R, Mahaffee WF, Pardyjak ER (2022) Quantifying turbulence heterogeneity in a vineyard using eddy-covariance and scintillometer measurements. Boundary-Layer Meteorol 184(3):479–504. https://doi.org/10.1007/s10546-022-00714-9

Petenko IV, Shurygin EA (1999) A two-regime model for the probability density function of the temperature structure parameter in the convective boundary layer. Boundary-Layer Meteorol 93(3):381–394. https://doi.org/10.1023/A:1002015522817

Petenko I, Mastrantonio G, Argentini S, Pietroni I, Viola A (2014) Some statistics of the temperature structure parameter in the convective boundary layer observed by sodar. Boundary-Layer Meteorol 150(2):215–233. https://doi.org/10.1007/s10546-013-9867-1

Petenko I, Casasanta G, Bucci S, Kallistratova M, Sozzi R, Argentini S (2020) Turbulence, low-level jets, and waves in the Tyrrhenian coastal zone as shown by sodar. Atmosphere 11(1):28. https://doi.org/10.3390/atmos11010028

Potter H, Lyu M, Yang X (2025) Elevated momentum flux in the surfzone during a storm. J Atmos Sci 82(7):1237–1247. https://doi.org/10.1175/JAS-D-24-0090.1

Savelyev SA, Taylor PA (2001) Notes on an internal boundary-layer height formula. Boundary-Layer Meteorol 101(2):293–301. https://doi.org/10.1023/A:1019208631216

Savelyev SA, Taylor PA (2005) Internal boundary layers: I. Height formulae for neutral and diabatic flows. Boundary-Layer Meteorol 115(1):1–25. https://doi.org/10.1007/s10546-004-2122-z

Sun J, Vandemark D, Mahrt L, Vickers D, Crawford T, Vogel C (2001) Momentum transfer over the coastal zone. J Geophys Res 106(D12):12437–12448. https://doi.org/10.1029/2000JD900696

Sykes RI, Henn DS, Lewellen WS (1993) Surface-layer description under free-convection conditions. Q J R Meteorol Soc 119(511):409–421. https://doi.org/10.1002/qj.49711951103

Tatarski VI (1961) Wave Propagation in a Turbulent Medium. Dover, 285 pp.

Vickers D, Mahrt L (1997) Fetch limited drag coefficients. Boundary-Layer Meteorol 85(1):53–79. https://doi.org/10.1023/A:1000472623187

Vickers D, Mahrt L (2010) Sea-surface roughness lengths in the midlatitude coastal zone. Q J R Meteorol Soc 136(649B):1089–1093. https://doi.org/10.1002/qj.617

Vickers D, Mahrt L, Sun J, Crawford T (2001) Structure of offshore flow. Mon Wea Rev 129(5):1251–1258

Vickers D, Mahrt L, Andreas EL (2013) Estimates of the 10-m neutral sea surface drag coefficient from aircraft eddy-covariance measurements. J Phys Oceanogr 43(2):301–310. https://doi.org/10.1175/JPO-D-12-0101.1

Wainwright CE, Bonin TA, Chilson PB, Gibbs JA, Fedorovich E, Palmer RD (2015) Methods for evaluating the temperature structure-function parameter using unmanned aerial systems and large-eddy simulation. Boundary-Layer Meteorol 155(2):189–208. https://doi.org/10.1007/s10546-014-0001-9
Wang Q, Alappattu DP, Billingsley S, Blomquist B, Burkholder RJ, Christman AJ, Creegan ED, de Paolo T, Eleuterio DP, Fernando HJS, Franklin KB, Grachev AA, Haack T, Hanley TR, Hocut CM, Holt TR, Horgan K, Jonsson HH, Hale RA, Kalogiros JA, Khelif D, Leo LS, Lind RJ, Lozovatsky I, Panella-Morato J, Mukherjee S, Nuss WA, Pozderac J, Rogers LT, Savelyev I, Savige DK, Shearman RK, Shen L, Terrill E, Ulate AM, Wang Q, Wendt RT, Wiss R, Woods RK, Xu L, Yamaguchi RT, Yardim C (2018) CASPER: coupled air-sea processes and electromagnetic (EM) wave ducting research. Bull Am Meteorol Soc 99(7):1449–1471. https://doi.org/10.1175/BAMS-D-16-0046.1
Wang S, Wang Q, Wauer BJ, Jiang Q (2020) Computing refractive index structure parameter Cn2 in a numerical weather prediction model. Geophys Res Lett 47(17):e2020GL089168. https://doi.org/10.1029/2020GL089168
Wang F, Du W, Yuan Q, Liu D, Feng S (2021) A survey of structure of atmospheric turbulence in atmosphere and related turbulent effects. Atmos 12(12):1608. https://doi.org/10.3390/atmos12121608
Wesely ML (1976) The combined effect of temperature and humidity fluctuations on refractive index. J Appl Meteor Climatol 15(1):43–49
Wilson JD (2015) Computing the flux footprint. Boundary-Layer Meteorol 156(1):1–14. https://doi.org/10.1007/s10546-015-0017-9
Wilson CJ, Fedorovich E (2012) Direct evaluation of refractive index structure functions from large-eddy simulation output for atmospheric convective boundary layers. Acta Geophys 60(5):1474–1492. https://doi.org/10.2478/s11600-012-0063-3
Wood CR, Kouznetsov RD, Gierens R, Nordbo A, Järvi L, Kallistratova MA, Kukkonen J (2013) On the temperature structure parameter and sensible heat flux over Helsinki from sonic anemometry and scintillometry. J Atmos Oceanic Technol 30(8):1604–1615. https://doi.org/10.1175/JTECH-D-12-00209.1
Wyngaard JC (2010) Turbulence in the atmosphere. Cambridge University Press, New York, p 393
Wyngaard JC, LeMone MA (1980) Behavior of the refractive index structure parameter in the entraining convective boundary layer. J Atmos Sci 37(7):1573–1585
Wyngaard JC, Izumi Y, Collins SA (1971) Behavior of the refractive-index structure parameter near the ground. J Opt Soc Am 61(12):1646–1650. https://doi.org/10.1364/JOSA.61.001646
Wyngaard JC, Pennell WT, Lenschow DH, LeMone MA (1978) The temperature-humidity covariance budget in the convective boundary layer. J Atmos Sci 35(1):47–58
Zilitinkevich SS, Hunt JCR, Esau IN, Grachev AA, Lalas DP, Akylas E, Tombrou M, Fairall CW, Fernando HJS, Baklanov AA, Joffre SM (2006) The influence of large convective eddies on the surface layer turbulence. Q J R Meteorol Soc 132(618A):1423–1456. https://doi.org/10.1256/qj.05.79

Authors and Affiliations

Andrey A. Grachev[1] · **Harindra J. S. Fernando**[2] · **Stef L. Bardoel**[2,3] · **Robb M. Randall**[1] · **Christopher M. Hocut**[1] · **Edward D. Creegan**[1] · **Laura S. Leo**[2,4]

✉ Andrey A. Grachev
andrey.a.grachev.civ@army.mil

1 Army Research Laboratory, WSMR, Las Cruces, NM 88002, USA

2 Department of Civil and Environmental Engineering and Earth Sciences, University of Notre Dame, Notre Dame, IN 46556, USA

3 Present Address: Department of Energy and Process Engineering, NTNU, 7491 Trondheim, Norway

4 Present Address: Department of Physics and Astronomy "Augusto Righi", University of Bologna, 40127 Bologna, Italy